

# Strain-Dependent Ionic Transport in $\text{Li}_3\text{YCl}_6$ Solid Electrolytes

Wei-Fan Huang,<sup>1,\*</sup> Jin Dai,<sup>1,\*</sup> Jiahui Pan,<sup>2</sup> and Mingjian Wen<sup>2,†</sup>

<sup>1</sup>*William A. Brookshire Department of Chemical and Biomolecular Engineering,  
University of Houston, Houston, TX, 77204, USA*

<sup>2</sup>*Institute of Fundamental and Frontier Sciences,  
University of Electronic Science and Technology of China, Chengdu, 611731, China*  
(Dated: May 8, 2026)

Solid-state batteries require electrolytes that sustain high ionic conductivity under the mechanical environment of a functioning cell. Lattice strain, arising from stack pressure, thermal cycling, or lattice mismatch at interfaces, can either enhance or suppress  $\text{Li}^+$  transport in solid electrolytes, yet how it couples to the underlying diffusion mechanism remains poorly understood. Using  $\text{Li}_3\text{YCl}_6$  halide superionic conductor, we address this with large-scale molecular dynamics simulations driven by an Atomic Cluster Expansion (ACE) machine learning interatomic potential trained on first-principles data. The ACE model faithfully reproduces experimental and *ab initio* structural, mechanical, and transport properties of  $\text{Li}_3\text{YCl}_6$ . We find that  $\text{Li}^+$  diffusion in  $\text{Li}_3\text{YCl}_6$  follows a two-regime Arrhenius behavior, crossing over at a critical temperature  $T_c$  from one-dimensional hopping at low temperature to three-dimensional cooperative diffusion at high temperature. Strain substantially modulates diffusivity: tensile strain enhances it while compressive strain suppresses it, yet leaves  $T_c$  invariant, indicating that strain tunes diffusion efficiency without reshaping the underlying transport framework. In each regime, the mechanistic origin differs: altered activation barriers dominate at low temperature, while modified pre-exponential factors become critical at high temperature. These results establish lattice strain as a design lever for ionic conductivity in  $\text{Li}_3\text{YCl}_6$  solid-state electrolytes.

## I. INTRODUCTION

Solid-state batteries (SSBs) are widely regarded as a promising successor to current lithium-ion technology, offering a pathway toward inherently safe and high-energy-density storage [1, 2]. Among the various technical requirements for high-performance SSBs, the ionic conductivity of the solid electrolyte (SE) stands as one of the most critical factors [3]. High ionic conductivity is a key enabler for achieving the power densities and fast-charging capabilities necessary for modern electric vehicles [4, 5]. Maintaining efficient lithium-ion mobility within a rigid solid framework is essential for leveraging the full potential of high-voltage cathodes and lithium metal anodes [6]. Consequently, extensive research has focused on discovering and optimizing superionic conductors that can facilitate rapid transport at room temperature [7, 8].

While high intrinsic ionic conductivity is a primary goal, the performance of these materials is often sensitive to the conditions encountered during cell integration. A significant challenge stems from the poor interfacial contact between the rigid SE and the electrode materials, which can lead to high interfacial resistance [7, 9–11]. To ensure mechanical integrity and continuous transport pathways, the application of external stack pressure is a common requirement in battery assembly [12–15]. However, this necessary pressure induces internal lattice strain and localized stress concentrations. Beyond stack

pressure, lattice strain can also arise from lattice mismatch at the electrode–electrolyte interface [16, 17] and from thermal cycling during battery operation [18, 19]. Because the movement of lithium ions is closely linked to the local atomic environment, these induced strain fields can directly modify the ionic transport properties of the material [14, 20, 21].

Understanding the mechanistic link between lattice strain and ionic conductivity remains a vital area of investigation. In crystalline halides and sulfides, ion transport is largely governed by the geometry of diffusion channels and the dynamic rigidity of the anion framework [22–24]. It is currently unclear whether the strain fields encountered in a practical battery enhance conductivity by widening migration paths or suppress it by rigidifying the lattice structure. Furthermore, the impact of strain on the critical temperature associated with superionic phase transitions is a fundamental question that remains largely unexplored. Establishing these relationships is necessary to develop design rules for engineering SEs that maintain optimal performance under the complex stress states of a functioning cell.

In this work, we investigate these transport-mechanics relationships using  $\text{Li}_3\text{YCl}_6$  as a representative prototype of high-performance halide electrolytes. Halide SEs have garnered attention due to their high ionic conductivity and favorable mechanical deformability [25–27].  $\text{Li}_3\text{YCl}_6$  is particularly suitable for this investigation because its transport mechanism undergoes a distinct transition from one-dimensional (1D) hopping to a three-dimensional (3D) cooperative diffusion regime at a critical temperature  $T_c$  [28, 29]. By applying isotropic strain in our simulations, we aim to quantify how mechanical

\* Equal contribution

† mjwen@uestc.edu.cn

distortion modulates these intrinsic pathways and the resulting conductivity.

To probe these phenomena with the necessary atomic-scale precision, we develop a machine learning interatomic potential based on the Atomic Cluster Expansion (ACE) framework [30, 31]. The ACE model is trained on density functional theory (DFT) data using the optB88-vdW functional to accurately capture the van der Waals interactions that dictate the rigidity of the anion lattice [32]. This approach enables us to perform large-scale molecular dynamics (MD) simulations to investigate the effects of isotropic strain on diffusivity and activation energy across a wide temperature range, beyond the capabilities of *ab initio* molecular dynamics (AIMD) that are typically limited to investigating small systems in the high-temperature regimes.

Our ACE model accurately reproduces the energetic, structural, mechanical, and transport properties of  $\text{Li}_3\text{YCl}_6$ , providing a robust foundation for investigating ionic transport under diverse mechanical environments. Using this framework, we demonstrate that while the critical temperature  $T_c$  is invariant under strain—confirming the two-regime diffusion as an intrinsic material property—the efficiency of transport is strongly strain-dependent. Specifically, tensile strain enhances diffusivity by boosting the pre-exponential factor  $D_0$  at low temperatures, and by simultaneously lowering activation barriers and further boosting  $D_0$  at elevated temperatures. In contrast, compressive strain suppresses transport by collapsing  $D_0$  across the full temperature range, compounded by increased activation barriers at high temperatures. These findings provide a high-level mechanistic understanding of how the mechanical environment tunes the efficiency of intrinsic diffusion rather than altering the fundamental transport framework. Ultimately, this study establishes that lattice strain is a powerful degree of freedom that can be exploited to optimize and sustain high ionic conductivity in halide-based solid-state batteries.

## II. MATERIALS AND METHODS

### A. $\text{Li}_3\text{YCl}_6$ Structures

$\text{Li}_3\text{YCl}_6$  has various polymorphs [33], and this work focuses on the trigonal phase and the orthorhombic phase. Both phases adopt a hexagonal close-packed anion sublattice of  $\text{Cl}^-$  anions, and they differ in the arrangements of  $\text{Li}^+$  and  $\text{Y}_3^+$  cations within the  $\text{Cl}^-$  framework [34]. The trigonal phase has a space group of  $\text{P}\bar{3}\text{m}1$ , which is isomorphic to  $\text{Li}_3\text{ErCl}_6$  (ICSD No. 50151), whereas the orthorhombic phase has a space group of  $\text{Pnma}$ , which is an isomorph of  $\text{Li}_3\text{YbCl}_6$  (ICSD No. 405610) [33]. Fig. 1 depicts the crystal structures of both phases. The  $\text{P}\bar{3}\text{m}1$  phase consists of 30 atoms in the conventional cell, where Li occupy Wyckoff sites 6g and 6h with typical occupancies of 100% and 50%, respectively [28]. The  $\text{Pnma}$  phase

consists of 40 atoms in the conventional cell, and Li atoms reside on the 8d sites [35].

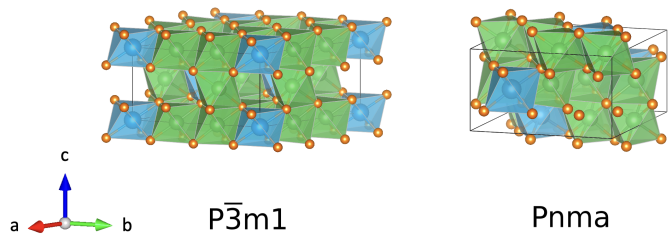


FIG. 1. **Crystal structures of  $\text{Li}_3\text{YCl}_6$ .** Cl, Li, and Y atoms are shown in orange, green, and blue, respectively.

### B. Atomic Cluster Expansion

We adopt the Atomic Cluster Expansion (ACE) interatomic potential [30, 31] to model the  $\text{Li}_3\text{YCl}_6$  system. ACE provides a complete basis for representing atomic environments and thus interatomic potential energy surfaces. It preserves fundamental physical symmetries, including translation, rotation, and inversion of space, as well as permutation of atomic species.

Within ACE, the total potential energy  $E$  of a system consisting of  $N$  atoms is constructed as a sum of the contributions of individual atoms:

$$E = \sum_{i=1}^N \epsilon_i, \quad (1)$$

where  $\epsilon_i$  denotes the energy of atom  $i$ . A description of the local environment of an atom is expressed as a linear combination of symmetry-adapted basis functions:

$$\varphi_i = \sum_{\nu} c_{\nu} B_{i\nu}, \quad (2)$$

where  $B_{i\nu}$  are basis functions constructed from radial and angular parts, which satisfy the symmetry requirements. The coefficients  $c_{\nu}$  are learnable parameters. For many-body interactions, the atomic energy is formulated as a nonlinear function  $\mathcal{F}$  of one or more such properties:

$$\epsilon_i = \mathcal{F}(\varphi_i^1, \varphi_i^2, \dots, \varphi_i^P), \quad (3)$$

where  $P$  is an index. A common strategy employing an EAM-like [36, 37] form uses only the first two terms:

$$\epsilon_i = \varphi_i^1 + \sqrt{\varphi_i^2}. \quad (4)$$

By systematically increasing the complexity of the basis set, the ACE framework provides controlled convergence toward the true potential energy surface, offering a robust and physically grounded representation of interatomic interactions. The ACE framework enables the construction of systematically improvable, highly accurate, and efficient machine learning interatomic potentials for large-scale atomistic simulations. A detailed discussion of the ACE framework is provided in Ref. [38].

### C. Development of ACE Potential

The ACE model was trained on DFT reference energies and forces using an active learning strategy for multiple rounds (Fig. 2). An initial dataset of  $\text{Li}_3\text{YCl}_6$  structures in both  $\text{P}\bar{3}\text{m1}$  and  $\text{Pnma}$  space groups was generated to train the first generation of models. The initial dataset consisted of three types of configurations: (1) relaxed structures and structures under strains of  $\pm 1$  and  $\pm 2\%$ ; (2) the relaxed and strained structures with perturbed atom positions, where the perturbation is drawn from a uniform distribution in the range 0 to 0.3 Å; and (3) structures sampled from AIMD trajectories at 500 K.

This led to an initial dataset of 2115 structures, whose total energy and atomic forces were obtained from DFT calculations. All DFT calculations were performed using the Vienna Ab initio Simulation Package (VASP) [39] and orchestrated by the `atomate2` [40] workflow engine. The default `atomate2` settings for VASP were adopted, except that the energy cutoff was set to 520 eV.

The first-generation ACE model was trained on the initial dataset. It was split into the training, validation, and test subsets with a ratio of 8:1:1. Model parameters were optimized using the training set by minimizing a loss function between the energy (and forces) predicted by ACE and the reference DFT values. Hyperparameters were determined by model performance on the validation set, and results are reported on the test set.

The trained first-generation ACE model was then continuously improved using an active learning strategy. This was achieved in three steps. First, MD simulations using the trained ACE model were performed for a maximum of 500000 steps. Second, for each snapshot (i.e., structure) along the MD trajectory, the *extrapolation grade*  $\gamma$  was calculated using the D-optimality criterion [41]. In general, a small  $\gamma$  means reliable interpolation, while a large  $\gamma$  suggests that the ACE model is performing extrapolation and thus the predictions become unreliable. Following Ref. [41], we employed two thresholds:  $\gamma_{\text{select}} = 2$  and  $\gamma_{\text{break}} = 10$ . Structures with  $\gamma < \gamma_{\text{select}}$  fall within the interpolation or accurate extrapolation region and require no intervention. A structure with  $\gamma > \gamma_{\text{break}}$  is flagged as risky extrapolation. Consequently, the MD simulation is terminated upon encountering such a structure, regardless of whether the 500000-step limit has been reached. Finally, structures in the intermediate range,  $\gamma_{\text{select}} \leq \gamma \leq \gamma_{\text{break}}$ , are classified as reliable extrapolations and are selected to enrich the dataset. The enriched dataset was then used to retrain the ACE model. This active learning loop continued until all snapshots along the MD trajectory achieved a  $\gamma$  smaller than  $\gamma_{\text{select}}$ . Further ACE fitting details such as hyperparameter search are provided in Section 1 in the Supplemental Material (SM).

## III. RESULTS AND DISCUSSION

### A. Validation of the Developed ACE Potential

TABLE I. **Comparison of computed and experimental lattice parameters.** The angles between the lattice vectors are  $\alpha = \beta = 90^\circ$  and  $\gamma = 120^\circ$  for the  $\text{P}\bar{3}\text{m1}$  phase, and  $\alpha = \beta = \gamma = 90^\circ$  for the  $\text{Pnma}$  phase. The DFT results without a reference are from this work.

	$a$ (Å)	$b$ (Å)	$c$ (Å)	Method
$\text{P}\bar{3}\text{m1}$	11.21	11.21	6.05	Exp. [28]
	11.03	11.03	6.09	DFT
	11.06	11.04	6.05	ACE
$\text{Pnma}$	12.93	11.12	6.04	Exp. [33]
	12.76	11.06	6.09	DFT
	12.83	11.03	6.10	ACE

The active learning loop proceeded for eight rounds, and the final ACE model was obtained using all data accumulated thus far. Fig. 3a and b show the extrapolation grade,  $\gamma$ , distributions for the first and final ACE models, respectively. For the first ACE model, although most configurations from the test set of the initial dataset exhibit  $\gamma$  values below 2, all configurations from the *active test set* (i.e., snapshots sampled from the MD trajectory) have  $\gamma$  values exceeding the selection threshold of 2. This suggested that the model was significantly extrapolating and became unreliable in the MD simulations. The model continued to be improved through active learning. For the final ACE model, all configurations from both the test set and the active test set have  $\gamma < 2$ , meaning that the model reliably interpolates or accurately extrapolates across the relevant configuration space.

The energy and forces predicted by the final ACE model closely match the DFT reference values, as shown in Fig. 3c and d. It achieves mean absolute errors (MAEs) of 0.52 meV/atom for energy and 14.09 meV/Å for forces on the test set. Energy and force MAEs for each generation of ACE models during active learning are summarized in Tables S1 and S2 in the SM. We also checked the structural properties predicted by the ACE model. The predicted lattice parameters of both  $\text{P}\bar{3}\text{m1}$  and  $\text{Pnma}$  phases closely match DFT and experimental results, with deviations within 0.5% (Table I).

In addition, we tested the model’s ability to predict mechanical properties by calculating the elastic tensor. The elastic tensor provides a fundamental and complete description of a material’s response to small deformations, capturing how stress and strain interrelate in different crystallographic directions [42].

The fourth-rank elastic tensor can be represented as a  $6 \times 6$  matrix using Voigt notation, where each component  $C_{ij}$  relates stress to strain in specific crystallographic directions [42]. It has up to 21 independent components in the most general case, but for crystals with inherent symmetry, the number of independent components reduces significantly. For  $\text{Li}_3\text{YCl}_6$ , the  $\text{P}\bar{3}\text{m1}$  phase that

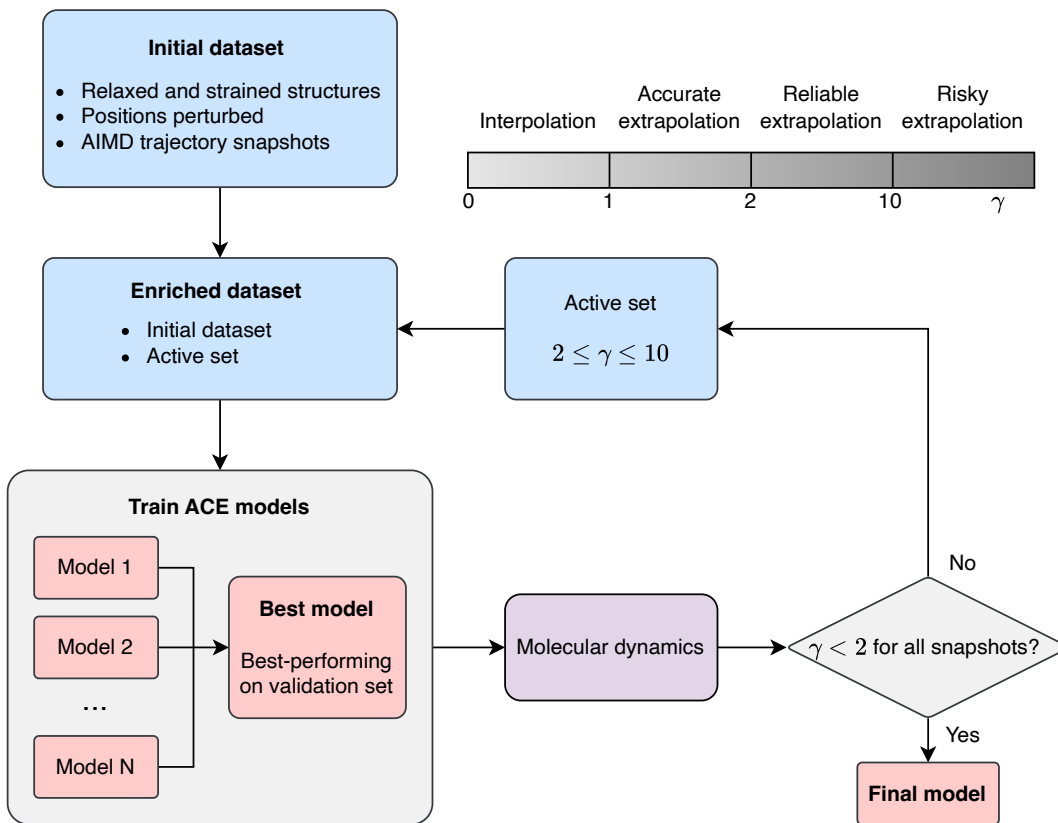


FIG. 2. **Active learning workflow to train ACE models for  $\text{Li}_3\text{YCl}_6$ .** With an initial dataset, the workflow iteratively improves model quality by adding new data for training. The loop stops when the extrapolation grade  $\gamma$  for all molecular dynamics snapshots is smaller than a threshold of 2.

belongs to the trigonal crystal system has six independent components, whereas the Pnma phase that belongs to the orthorhombic crystal system has nine independent components [43]. Fig. 4 illustrates the independent components and their symmetry-induced relationships.

We compute the elastic tensors with the finite difference method [40] using ACE and compare with DFT calculations. The results are summarized in Table II. The elastic tensor predicted by ACE closely matches those obtained from DFT using the same underlying optB88-vdW functional, with a maximum deviation of 10% for  $C_{15}$  in the P3m1 phase ( $-1.7$  vs  $-1.9$  GPa). For the other components, the deviation is even smaller (within 5%), which represents good agreement given the complexity of the elastic tensor and the fact that it was not explicitly included in the training dataset. In addition to the individual elastic tensor components, we also derive key mechanical moduli that characterize the material’s response to various deformation modes. Specifically, we computed the bulk modulus ( $B$ ), shear modulus ( $G$ ), and Young’s modulus ( $E$ ) using the Hill averaging scheme [42] (computing procedures provided in the SM). Given that the individual components of the elastic tensor are accurately reproduced, as expected the derived moduli also exhibit strong agreement between ACE predictions and

DFT calculations.

These validation tests confirmed that the developed ACE model accurately reproduces the energetic, structural, and elastic properties of  $\text{Li}_3\text{YCl}_6$  from both experiments and DFT calculations. In the following sections, we employ the validated ACE model to perform large-scale MD simulations to investigate the  $\text{Li}^+$  transport behavior of  $\text{Li}_3\text{YCl}_6$ , which is critical for its performance as a solid-state electrolyte.

## B. $\text{Li}^+$ Transport

Ionic conductivity governs  $\text{Li}^+$  transport kinetics and dictates both the power capability and energy efficiency of solid-state batteries [4, 8]. Consequently, numerous computational efforts using AIMD have been devoted to quantifying the ionic conductivity of  $\text{Li}_3\text{YCl}_6$  at ambient temperatures [46–49]. However, these studies are often compromised by three primary methodological limitations that undermine their accuracy. First, room-temperature estimates largely rely on extrapolations from high-temperature simulations, a practice that can overlook transitions in diffusion mechanisms [50, 51]. Second, many simulations are restricted to short trajectory-

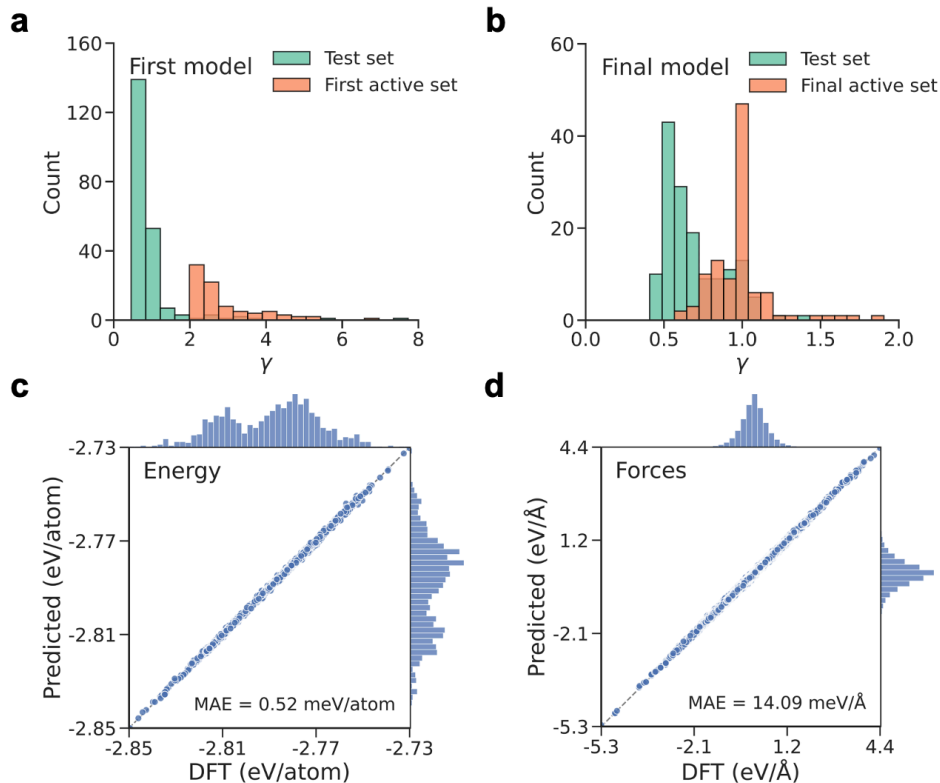


FIG. 3. **Performance of the developed ACE model.** Histogram of the maximum extrapolation grade  $\gamma_{\max}$  in the active learning loop: (a) first model and (b) final model. ACE predicted versus DFT reference (c) energy and (d) atomic forces on the test set obtained using the final ACE model.

TABLE II. **Computed elastic tensors and the derived elastic moduli.** The components of the elastic tensor  $C_{ij}$  and the bulk modulus  $B$ , shear modulus  $G$ , and Young’s modulus  $E$  are reported in GPa. Only independent  $C_{ij}$  components are listed; others can be obtained by symmetry as shown in Fig. 4. The DFT results without a reference are from this work.

	$C_{11}$	$C_{12}$	$C_{13}$	$C_{15}$	$C_{22}$	$C_{23}$	$C_{33}$	$C_{44}$	$C_{55}$	$C_{66}$	$B$	$G$	$E$	Method
P $\bar{3}$ m1	50.5	18.5	6.8	-2.5			40.8	12.6			22.5	15.0	35.0	DFT (PBE) [44]
	48.1	18.2	10.9	-0.1			37.8	15.0			28.2	15.0	38.1	DFT (PBE) [45]
	54.4	19.9	13.6	-1.9			43.2	13.2			27.0	15.4	38.8	DFT
	54.7	20.4	13.1	-1.7			41.4	13.7			26.6	15.6	39.2	ACE
Pnma	52.4	18.7	12.6		51.5	11.8	39.4	12.2	11.4	16.4	25.1	14.3	36.2	DFT
	53.5	19.0	12.3		52.9	12.5	38.6	12.9	11.6	16.9	25.3	14.7	37.0	ACE

ries of  $\sim 100$  ps and small supercells of  $\sim 100$  atoms; these scales are insufficient to statistically resolve long-range lithium-ion migration or capture representative bulk behavior [46–49]. Third, several investigations were conducted at temperatures exceeding the material’s 800 K melting point, potentially introducing liquid-like dynamics that do not reflect the physics of a solid-state conductor [25, 50]. Collectively, these constraints introduce significant uncertainty and may lead to inaccurate assessments of the material’s performance.

To overcome the aforementioned limitations, we performed large-scale MD simulations using the developed ACE model. The ACE model provides the necessary computational efficiency to simulate large systems and extended timescales while maintaining near-first-

principles accuracy, effectively bridging the gap between accuracy and computational efficiency. Specifically, we employed  $3 \times 3 \times 6$  supercells, containing 1620 atoms for the P $\bar{3}$ m1 phase and 2160 atoms for the Pnma phase, and extended the simulation time to 20 ns. The simulations were performed using the Large-scale Atomic/Molecular Massively Parallel Simulator (LAMMPS) [52] under the NVT ensemble using a Nosé–Hoover thermostat with a timestep of 1 fs. By performing these simulations across a wide temperature range (300–800 K), we eliminate the need for high-temperature extrapolation and ensure all data points remain below the material’s melting point to maintain solid-state integrity. The self-diffusion coefficient  $D$  was computed using the Einstein relation [53], which links the mean squared displacement (MSD) of the

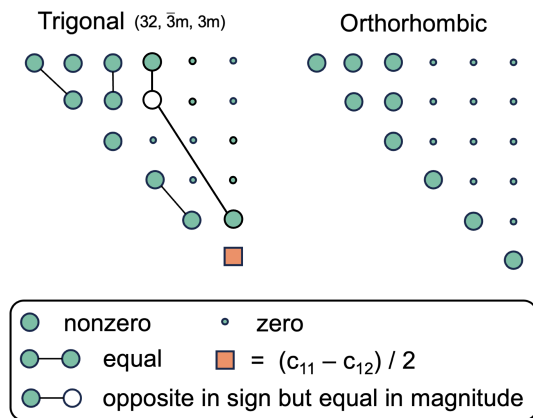


FIG. 4. **Independent components of the elastic tensor of  $\text{Li}_3\text{YCl}_6$ .** The trigonal  $\text{P}\bar{3}\text{m}1$  phase and orthorhombic  $\text{Pnma}$  phase have six and nine independent components, respectively. Only the upper triangular part of the elastic tensor is shown, and the lower triangular part can be obtained by symmetry, i.e.,  $C_{ij} = C_{ji}$ .

lithium ions to the simulation time. From the calculated diffusivity, ionic conductivity  $\sigma$  can be derived using the Nernst–Einstein equation [54]. Calculation details are provided in the SM.

To investigate the effect of temperature  $T$  on  $\text{Li}^+$  diffusion, we plot the diffusivity  $D$  as a function of  $T$  for both the  $\text{P}\bar{3}\text{m}1$  and  $\text{Pnma}$  phases in Fig. 5. The computed  $D$  using our ACE model trained on the optB88-vdW DFT data [32, 58] follows the Arrhenius relationship [59]:

$$D = D_0 \exp\left(-\frac{E_a}{k_B T}\right), \quad (5)$$

where  $D_0$  is a pre-exponential factor,  $k_B$  is the Boltzmann constant,  $T$  is the temperature, and  $E_a$  is the activation energy for  $\text{Li}^+$  diffusion. In other words, the logarithm of  $D$  exhibits a linear relationship with  $1/T$ , where the slope is proportional to  $E_a$ . However, this linear relationship is not observed across the entire temperature range; instead, we observe a two-regime behavior characterized by a sharp change in  $E_a$  (values given in Table III) at a critical temperature  $T_c$  of 425 K for the  $\text{P}\bar{3}\text{m}1$  phase and 380 K for the  $\text{Pnma}$  phase. Our ACE predictions agree well with literature data, particularly with experimental measurements in the room-temperature regime. For example, the computed  $E_a$  is 0.35 eV for the  $\text{P}\bar{3}\text{m}1$  phase in the low-temperature regime ( $T < T_c$ ), which is in good agreement with experimental values in the range of 0.40–0.51 eV [25, 55, 56].

The two-regime behavior in the Arrhenius plot indicates a transition in the dominant  $\text{Li}^+$  diffusion mechanism at  $T_c$ . This is consistent with prior observations [28, 48, 51].  $\text{Li}^+$  migration in  $\text{Li}_3\text{YCl}_6$  is governed by two distinct intrinsic diffusion pathways: (1) the direct octahedral–octahedral (Oct–Oct) hop that requires no intermediate sites (Fig. 6a), and (2) the cooperative octahedral–tetrahedral–octahedral (Oct–Tet–Oct)

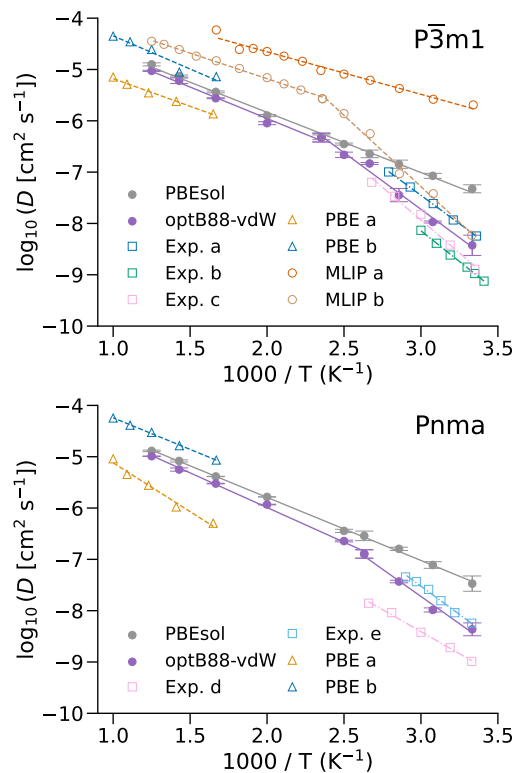


FIG. 5. **Arrhenius plot of the  $\text{Li}^+$  diffusivity  $D$ .** Filled symbols represent results from this work, using ACE trained on DFT data with different functionals (optB88-vdW and PBEsol). Open symbols represent literature data. Experimental values: a [25], b [55], c [56], d [48] and e [57]; AIMD simulations (PBE a [48] and PBE b [47]); classical MD simulations using MLIPs (MLIP a, fitted to PBE DFT data) [29] and (MLIP b, fitted to optB88-vdW DFT data) [29]. Error bars represent standard deviations from 3 independent MD runs.

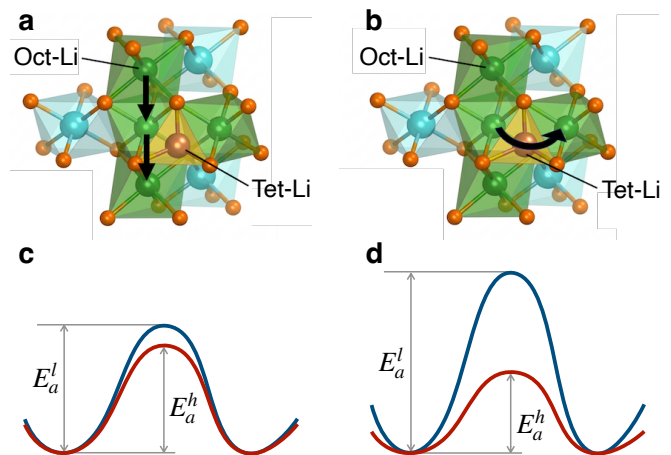


FIG. 6. **Schematic illustration of the  $\text{Li}^+$  diffusion pathways.** Diffusion pathways along the (a) Oct–Oct sites and (b) Oct–Tet–Oct sites in the  $\text{P}\bar{3}\text{m}1$  phase. Activation energies at low temperature ( $E_a^l$ ) and high temperature ( $E_a^h$ ) for the (c) Oct–Oct and (d) Oct–Tet–Oct pathways.

TABLE III. **Comparison of the Li ionic conductivity  $\sigma$  and activation energy  $E_a$  in  $\text{Li}_3\text{YCl}_6$ .** In the table, MD refers to classical MD simulation using interatomic potentials derived from DFT calculations. Ionic conductivity  $\sigma$  is reported at a temperature ( $T$ ) of 300 K, and † indicates extrapolated values from high-temperature simulations.

Phase	$\sigma$ (mS/cm)	$E_a$ (eV)	$T$ (K)	Method
P $\bar{3}m1$	0.51	0.40	240–360	Exp. [25]
	0.10	0.45	233–333	Exp. [55]
	0.11	0.51	300–373	Exp. [56]
	12.17†	0.24	400–700	AIMD (PBE) [56]
	14.00†	0.19	500–900	AIMD (PBE) [46]
	3.07†	0.15	600–1000	AIMD (PBE) [48]
		0.26	600–1000	AIMD (PBE) [47]
	0.12†	0.37	700–1000	AIMD (optB86b-vdW) [49]
	152.66	0.16	300–800	MD (PBE) [29]
	0.56	0.49	300–425	MD (optB88-vdW) [29]
		0.24	425–800	MD (optB88-vdW) [29]
	0.02†	0.80	375–425	MD (optB88-vdW) [50]
		0.23	425–800	MD (optB88-vdW) [50]
	0.02†	0.74	330–425	MD (optB88-vdW) [51]
		0.24	425–700	MD (optB88-vdW) [51]
Pnma	4.21	0.23	300–800	MD (PBEsol)
	0.77	0.35	300–425	MD (optB88-vdW)
		0.25	425–800	MD (optB88-vdW)
	0.09	0.31	300–370	Exp. [48]
	0.50	0.36	300–348	Exp. [57]
	0.04†	0.31	600–1000	AIMD (PBE) [48]
		0.24	600–1000	AIMD (PBE) [47]
		0.69	300–380	MD (optB88-vdW) [51]
		0.21	380–700	MD (optB88-vdW) [51]
	2.96	0.24	300–800	MD (PBEsol)
0.88	0.30	300–380	MD (optB88-vdW)	
	0.28	380–800	MD (optB88-vdW)	

hop that proceeds through the tetrahedral intermediate site (Fig. 6b). At low temperature  $T < T_c$ , the formation energy of  $\text{Li}^+$  occupying the Tet intermediate sites is high. This results in a prohibitively high activation barrier for the Oct–Tet–Oct pathway ( $E_a^l$  in Fig. 6d), making it inaccessible [60]. As a result,  $\text{Li}^+$  migration is restricted exclusively to the Oct–Oct pathway, which has a lower intrinsic activation energy ( $E_a^l$  in Fig. 6c), and thus defines the apparent  $E_a = 0.35$  eV in this regime. At high temperature  $T > T_c$ , thermal energy overcomes the formation energy of Tet intermediate sites, substantially lowering the activation energy of the Oct–Tet–Oct pathway ( $E_a^h$  in Fig. 6d). This drives a transition to the Oct–Tet–Oct pathway as the dominant transport mechanism.

We support these mechanistic arguments with the  $\text{Li}^+$  probability density map, which shows the likelihood of finding an  $\text{Li}^+$  ion at each location in the simulation cell along the MD trajectory (generation method given in SM). At 300 K, the map for P $\bar{3}m1$  in Fig. 7a shows  $\text{Li}^+$  density concentrated almost entirely at the Oct sites. Vertical Oct–Oct hopping is already active at this

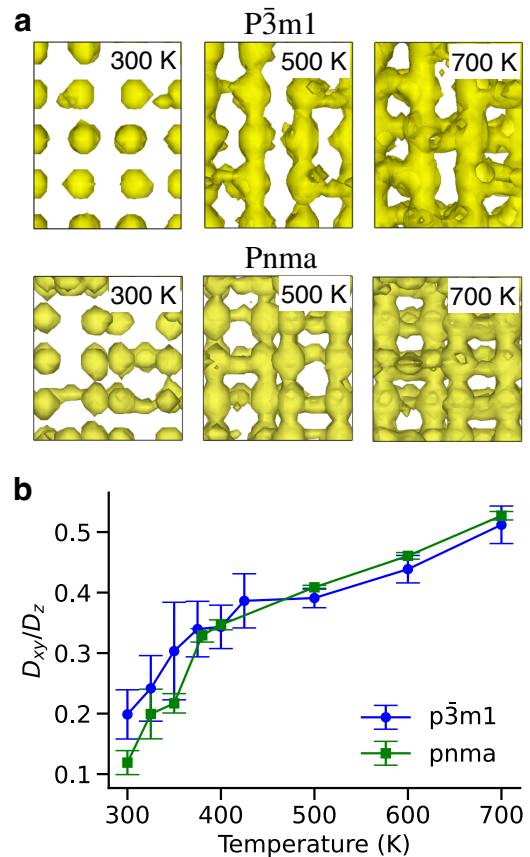


FIG. 7. **Contribution of different diffusion pathways to the overall  $\text{Li}^+$  transport.** (a)  $\text{Li}^+$  probability density showing the trajectory of  $\text{Li}^+$  ions during MD simulations, viewed from the *b-c* plane in Fig. 1. (b) Ratio of the diffusivity along the Oct–Tet–Oct pathway  $D_{xy}$  to that along the Oct–Oct pathway  $D_z$ .

temperature, as evidenced by the nonzero diffusivity in Fig. 5, but the events are too infrequent to produce visible density in the map. As the temperature increases to 500 K, continuous one-dimensional channels emerge along the vertical direction via Oct–Oct hopping, and horizontal Oct–Tet–Oct bridges also appear. Although less pronounced than the vertical channels, they are already sufficient to link the 1D channels into a three-dimensional network. At 700 K, the horizontal Oct–Tet–Oct pathways become more pronounced and contribute an increasingly large share of the overall  $\text{Li}^+$  transport. To quantitatively assess the relative contributions of the two pathways, we compute  $D_{xy}$  and  $D_z$  by isolating the *xy* and *z* components of the  $\text{Li}^+$  diffusivity, respectively, and plot their ratio in Fig. 7b. The ratio rises monotonically from  $\sim 0.2$  at 300 K to  $\sim 0.55$  at 700 K, confirming that the thermally activated opening of Oct–Tet–Oct pathways progressively enhances the transverse contribution to  $\text{Li}^+$  diffusion.

Why does the formation energy of Tet sites decrease so markedly with temperature such that the Oct–Tet–Oct

pathway becomes more pronounced above  $T_c$ ? This originates from the intrinsic temperature-dependent rigidity of the  $\text{Cl}^-$  anion lattice in  $\text{Li}_3\text{YCl}_6$ , which is governed by long-range van der Waals (vdW) dispersion forces between neighboring  $\text{Cl}^-$  ions [29, 61]. At temperatures below  $T_c$ , the  $\text{Cl}^-$  lattice is stabilized by vdW interactions and remains rigid, resisting local distortion. Above  $T_c$ , thermal fluctuations are sufficiently strong to soften the anion lattice by partially overcoming the cohesive vdW forces that bind adjacent  $\text{Cl}^-$  ions together. These thermal motions (lattice vibrations and atomic displacements) create transient free volume within the anion framework, reducing the energy penalty required to push  $\text{Cl}^-$  ions apart and form a Tet intermediate site. This weakening of vdW cohesion directly reduces the formation energy of Tet intermediate sites, as the lattice is no longer rigidly locked into its low-temperature configuration and can accommodate the local distortion needed to stabilize the Tet site. This in turn lowers the activation barrier of the cooperative Oct–Tet–Oct pathway, allowing it to become the dominant diffusion mechanism.

Therefore, the correct description of the two-regime behavior in the Arrhenius plot is critically dependent on the accurate treatment of vdW forces. For this reason, we selected the optB88-vdW functional to generate the training data for our ACE model, as it explicitly accounts for vdW interactions in its functional form. To further confirm the critical role of vdW forces, we also trained ACE models using data generated with the PBEsol functional [62], which is a widely used GGA functional that does not account for vdW interactions (model performance given in Table S3 in the SM). As shown in Fig. 5, the ACE model trained on PBEsol data exhibits qualitatively different behavior, with a single linear Arrhenius relationship across the entire temperature range and no evidence of a transition at  $T_c$ . In contrast to optB88-vdW, PBEsol fails to capture the long-range vdW cohesion that stabilizes the rigid anion lattice at low temperatures, leading to an unphysically soft lattice description at all temperatures [63, 64]. This artificial softness means Tet intermediate sites exhibit minimal formation energy even at low temperatures, so the activation barrier of the Oct–Tet–Oct pathway remains low across the entire temperature range.

This analysis explains why many AIMD and classical MD simulations in the literature fail to yield the correct ionic conductivity  $\sigma$  of  $\text{Li}_3\text{YCl}_6$ . AIMD simulations are typically performed at high temperatures to accelerate  $\text{Li}^+$  diffusion and obtain sufficient statistics within computationally feasible timescales. The room-temperature  $\sigma$  is then extrapolated from the high-temperature data using a single linear Arrhenius relationship [46–48, 56], which overlooks the critical transition at  $T_c$  and thus overestimates  $D$  and the resultant  $\sigma$  when compared with the experimental data (see Table III). Classical MD simulations using interatomic potentials fitted to PBE or PBEsol data also fail to capture the correct two-regime behavior, as the underlying functional does not

TABLE IV. **Strain-dependent ionic conductivity and activation energy.** Ionic conductivity  $\sigma$  is reported in mS/cm at  $T = 300$  K. The critical temperature is  $T_c = 425$  K for  $\text{P}\bar{3}\text{m}1$  and 380 K for  $\text{Pnma}$ , and the activation energies (in eV)  $E_a$  are reported separately for the low-temperature ( $T < T_c$ ) and high-temperature ( $T > T_c$ ) regimes.

	Strain	$\sigma$	$E_a(T < T_c)$	$E_a(T > T_c)$
$\text{P}\bar{3}\text{m}1$	-2%	0.38	0.26	0.32
	-1%	0.61	0.27	0.30
	0%	0.77	0.35	0.25
	1%	0.78	0.39	0.24
	2%	1.13	0.42	0.20
$\text{Pnma}$	-2%	0.66	0.19	0.30
	-1%	0.82	0.23	0.30
	0%	0.88	0.30	0.28
	1%	1.36	0.36	0.23
	2%	2.25	0.43	0.19

account for vdW interactions and thus cannot describe the temperature-dependent lattice rigidity that governs the transition in diffusion mechanisms. They overestimate  $\sigma$  at room temperature as well, as seen in both our ACE model trained on PBEsol data and the literature MLIP fitted to PBE data [29] (see Table III).

### C. Strain Effect

To investigate the effects of strain on the  $\text{Li}^+$  transport behavior in  $\text{Li}_3\text{YCl}_6$ , we perform MD simulations under isotropic compressive and tensile strains ranging from -2% to 2%. Assuming linear elasticity and using the elastic tensors computed in Section III A, a 2% isotropic strain corresponds to a maximum stress of about 1.7 GPa for both the  $\text{P}\bar{3}\text{m}1$  and  $\text{Pnma}$  phases (calculation given in SM). This nominal stress exceeds the typical stack pressure applied in experiments, which is on the order of tens to hundreds of MPa [65–67]; however, the actual internal stress can be significantly higher due to interfacial roughness, microstructural heterogeneity, and stress concentrations [68, 69], making the selected strain range relevant to practical battery conditions.

The effect of strain on the diffusivity is shown in Fig. 8. Positive tensile strains shift the curves upward compared to the unstrained case across the entire temperature range, indicating higher diffusivity  $D$  and ionic conductivity  $\sigma$ . Conversely, negative compressive strains shift the curves downward, leading to lower  $D$  and  $\sigma$  (values given in Table IV). The two-regime behavior of the Arrhenius plot observed in the unstrained case is preserved under both tensile and compressive strains, and the transition temperatures  $T_c$  remain unchanged: 425 K for the  $\text{P}\bar{3}\text{m}1$  phase and 380 K for the  $\text{Pnma}$  phase. The invariance of  $T_c$  suggests that strain does not alter the underlying diffusion mechanism of  $\text{Li}_3\text{YCl}_6$ . However, the slope of the Arrhenius curves in the two regimes is modified in a different manner, indicating that strain modulates the efficiency and accessibility of the diffusion pathways in a

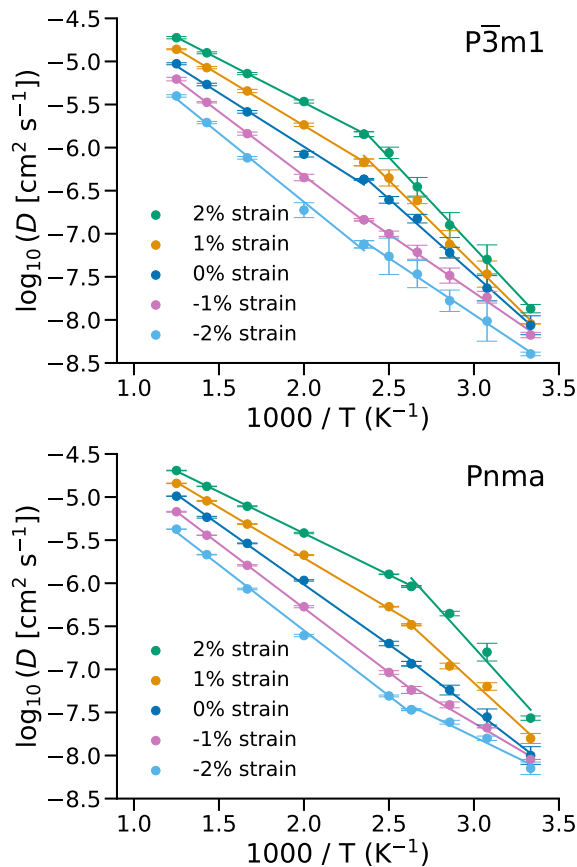


FIG. 8. Arrhenius plot of the Li diffusivity  $D$  of  $\text{Li}_3\text{YCl}_6$  under strain. Shown for strain conditions ranging from  $-2\%$  to  $2\%$ , using the potential with active set from seven active learning cycles based on the optB88-vdW functional.

temperature-dependent manner.

In the low-temperature regime  $T < T_c$ , tensile strain induces a counterintuitive trend: the activation energy  $E_a$  increases with the strain magnitude, while the diffusivity  $D$  remains higher than the unstrained case (Fig. 8). This behavior is driven by the pre-exponential factor  $D_0$  in Eq. (5), whose increase overcompensates for the cost of a higher  $E_a$ . As discussed in Section III B, the dominant diffusion pathway in the low-temperature regime for unstrained  $\text{Li}_3\text{YCl}_6$  is the direct Oct–Oct hop; the multistep Oct–Tet–Oct pathway is restricted due to the high formation energy of Tet intermediate sites. Tensile strain leads to lattice expansion and thus reduces the formation energy of Li occupying the Tet sites, resulting in a significant increase in Tet site occupancy even at low temperatures. This is directly confirmed by Fig. 9a: the  $\text{Li}^+$  probability density at 300 K becomes progressively more delocalized with increasing tensile strain, with additional horizontal Oct–Tet–Oct diffusion channels emerging at 2% strain. Fig. 9b quantifies this further using the  $\text{Li}^+$  site occupancy fraction (calculation details in SM): at 300 K, 2% tensile strain produces a  $\sim 3\times$  increase in

Tet site occupancy relative to the unstrained case, while Oct site occupancy decreases by  $\sim 6\%$ . The activated Oct–Tet–Oct pathways have a higher intrinsic activation energy than the direct Oct–Oct pathway, thus raising the overall  $E_a$ . Tensile strain also drives a dramatic change in the pre-exponential factor [70] in Eq. (5):

$$D_0 = \frac{1}{z} a_0^2 \nu \exp\left(\frac{\Delta S_m}{k_B}\right), \quad (6)$$

where  $z$  is the number of nearest-neighbor jump sites,  $a_0$  is the effective jump distance,  $\nu$  is the vibrational attempt frequency, and  $\Delta S_m$  is the migration entropy. Specifically, the expanded lattice increases the effective jump distance  $a_0$  and increases the migration entropy  $\Delta S_m$  by rendering additional  $\text{Li}^+$  sites accessible (such as Tet sites discussed above); moreover, it weakens spatial confinement from the anion framework, allowing more frequent  $\text{Li}^+$  vibrations and thus increasing the attempt frequency  $\nu$ . These combined effects significantly boost  $D_0$ , which more than offsets the cost of a higher  $E_a$  and results in an overall enhancement of  $D$  under tensile strain.

In the high-temperature regime ( $T > T_c$ ), tensile strain produces a synergistic enhancement of  $\text{Li}^+$  diffusivity by simultaneously reducing the activation energy  $E_a$  and boosting the pre-exponential factor  $D_0$ . As discussed in Section III B, the high thermal energy at  $T > T_c$  already overcomes the formation energy of Tet intermediate sites, making the cooperative Oct–Tet–Oct pathway the dominant diffusion mechanism in unstrained  $\text{Li}_3\text{YCl}_6$ , which yields an intrinsically low activation energy  $E_a$ . Lattice expansion induced by tensile strain further lowers this intrinsic barrier. For example,  $E_a$  falls from 0.25 eV at 0% strain to 0.20 eV at 2% strain for P3m1 (Table IV). In parallel, the expanded lattice enhances  $D_0$  via the same mechanistic drivers identified in the low-temperature regime, with an even stronger effect due to the already high accessibility of Tet sites at  $T > T_c$ . Our atomistic simulation data validate this: Fig. 9b shows elevated Tet site occupancy under 2% strain relative to the unstrained system at 700 K, and Fig. 9a reveals a more open, well-connected 3D  $\text{Li}^+$  diffusion network. The combined reduction in  $E_a$  and enhancement of  $D_0$  deliver the strongest improvement of  $D$  under tensile strain at elevated temperatures.

Under compressive strain, the characteristic upward-bent curves seen in the unstrained and tensile cases are replaced by distinct downward-bent curves (Fig. 8). In the low-temperature regime ( $T < T_c$ ), compressive strain reduces the apparent activation energy  $E_a$  (e.g., from 0.35 eV at 0% strain to 0.26 eV at  $-2\%$  strain for P3m1, Table IV), yet significantly suppresses total  $D$  relative to the unstrained system. This counterintuitive trend arises from a dramatic collapse of the pre-exponential factor  $D_0$ , whose reduction fully overwhelms the minor benefit of a lower  $E_a$ . Lattice contraction rigidifies the anion framework, renders intermediate Tet sites energetically inaccessible—Tet site occupancy remains negligible and does not increase from 300 K to 400 K under  $-2\%$

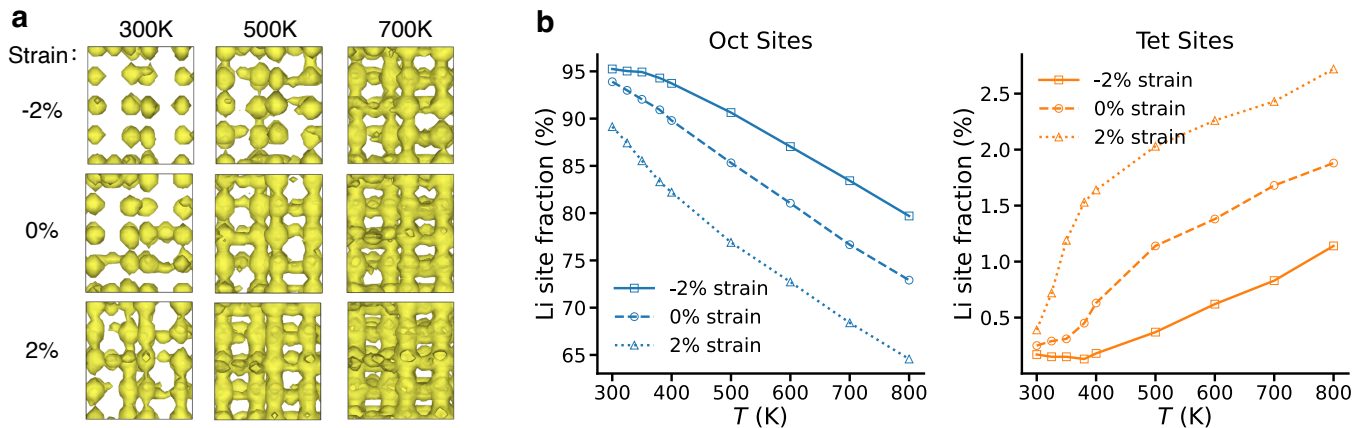


FIG. 9. **Effect of strain on the  $\text{Li}^+$  transport behavior in  $\text{Pnma Li}_3\text{YCl}_6$ .** (a)  $\text{Li}^+$  probability density at different strains and temperatures, viewed from the  $b$ - $c$  plane in Fig. 1. (b)  $\text{Li}^+$  occupancy fraction for the octahedral (Oct) and tetrahedral (Tet) sites at different temperatures.

strain as shown in Fig. 9b. Diffusion is therefore confined to the Oct–Oct pathway, as confirmed by the localized  $\text{Li}^+$  probability density at 300 K under  $-2\%$  strain in Fig. 9a, reversing the  $D_0$ -boosting mechanisms identified in the tensile strain analysis. In the high-temperature regime ( $T > T_c$ ), compressive strain reduces the Tet site occupancy and disrupts the percolation of the 3D Oct–Tet–Oct diffusion network ( $-2\%$  data at 700 K in Fig. 9b, c). Consequently, it exerts a dual suppressive effect on  $\text{Li}^+$  transport by simultaneously increasing the activation energy  $E_a$  and reducing the pre-exponential factor  $D_0$ .

#### IV. CONCLUSIONS

This work develops an accurate and efficient machine learning interatomic potential (ACE) for the  $\text{Li}_3\text{YCl}_6$  solid-state electrolyte, trained on DFT data that explicitly accounts for van der Waals interactions. Verification tests against DFT calculations and experimental data confirm that our ACE model accurately captures the structural, mechanical, and transport properties of  $\text{Li}_3\text{YCl}_6$ . We find that the correct description of the temperature dependence of  $\text{Li}^+$  diffusivity is critically dependent on the accurate treatment of vdW forces, as they govern the intrinsic temperature-dependent rigidity of the anion lattice and thus the transition in dominant diffusion mechanisms.

Our study reveals two fundamental, mechanistically consistent insights into strain-tunable  $\text{Li}^+$  transport in  $\text{Li}_3\text{YCl}_6$ . First, the invariance of the critical temperature  $T_c$  across tensile and compressive loading confirms that the core physical origin of the two-regime diffusion behavior is an intrinsic property of the material, not an artifact of simulation. Applied strain only modulates the efficiency, accessibility, and entropic drivers of the two core diffusion pathways, rather than altering the funda-

mental diffusion framework or introducing new transport mechanisms. Second, the mechanism of strain tuning is inherently coupled to the dominant diffusion pathway, and thus strongly temperature-dependent. Tensile strain enhances diffusivity via an increased pre-exponential factor  $D_0$  at low temperatures, and via synergistic reductions in  $E_a$  and increases in  $D_0$  at high temperatures; compressive strain suppresses transport via  $D_0$  reduction at low temperatures, and via simultaneous increases in  $E_a$  and reductions in  $D_0$  at high temperatures.

These findings have critical implications for the design and operation of solid-state batteries. While external stack pressure is widely applied to maintain interfacial contact between the solid electrolyte and electrodes, our results demonstrate that excessive pressure can induce detrimental compressive strain in the  $\text{Li}_3\text{YCl}_6$  lattice, suppressing ionic conductivity across the full operating temperature range of the battery. Conversely, our results suggest that controlled tensile strain in the electrolyte, while challenging to implement in practice, offers a viable route to enhance  $\text{Li}^+$  transport. This work bridges atomic-scale lattice strain effects and macroscale ionic transport behavior, providing clear mechanistic insights and design rules for tailoring the mechanical response and ionic conductivity of halide solid electrolytes in practical solid-state battery systems.

#### DATA AND CODE AVAILABILITY

The dataset used in this work, along with the scripts for model training, molecular dynamics simulations, and data analysis, is publicly available at [https://github.com/weifanfrank/mlip\\_halide\\_electrolytes](https://github.com/weifanfrank/mlip_halide_electrolytes). The ACE models are trained using **pacemaker**, which can be accessed at <https://github.com/ICAMS/python-ace>.

## ACKNOWLEDGEMENTS

This work is supported by the National Science Foundation under Grant No. 2316667 and the Research Computing Data Core at the University of Houston. It uses computational resources provided by the Hefei Advanced Computing Center.

- 
- [1] J. Janek and W. G. Zeier, A solid future for battery development, *Nature Energy* **1**, 10.1038/nenergy.2016.141 (2016).
- [2] A. Manthiram, X. Yu, and S. Wang, Lithium battery chemistries enabled by solid-state electrolytes, *Nature Reviews Materials* **2**, 10.1038/natrevmats.2016.103 (2017).
- [3] T. Famprikis, P. Canepa, J. A. Dawson, M. S. Islam, and C. Masquelier, Fundamentals of inorganic solid-state electrolytes for batteries, *Nature Materials* **18**, 1278 (2019).
- [4] J. C. Bachman, S. Muy, A. Grimaud, H.-H. Chang, N. Pour, S. F. Lux, O. Paschos, F. Maglia, S. Lupart, P. Lamp, L. Giordano, and Y. Shao-Horn, Inorganic solid-state electrolytes for lithium batteries: Mechanisms and properties governing ion conduction, *Chemical Reviews* **116**, 140 (2016).
- [5] P. Albertus, V. Anandan, C. Ban, N. Balsara, I. Belharouak, J. Buettner-Garrett, Z. Chen, C. Daniel, M. Doeff, N. J. Dudney, B. Dunn, S. J. Harris, S. Herle, E. Herbert, S. Kalnaus, J. A. Libera, D. Lu, S. Martin, B. D. McCloskey, M. T. McDowell, Y. S. Meng, J. Nanda, J. Sakamoto, E. C. Self, S. Tepavcevic, E. Wachsman, C. Wang, A. S. Westover, J. Xiao, and T. Yersak, Challenges for and pathways toward li-metal-based all-solid-state batteries, *ACS Energy Letters* , 1399 (2021).
- [6] M. A. Kraft, S. P. Culver, M. Calderon, F. Böcher, T. Krauskopf, A. Senyshyn, C. Dietrich, A. Zevalkink, J. Janek, and W. G. Zeier, Influence of lattice polarizability on the ionic conductivity in the lithium superionic argyrodites  $\text{Li}_6\text{PS}_5\text{X}$  ( $\text{X} = \text{Cl}, \text{Br}, \text{I}$ ), *Journal of the American Chemical Society* **139**, 10909 (2017).
- [7] Y. Xiao, Y. Wang, S.-H. Bo, J. C. Kim, L. J. Miara, and G. Ceder, Understanding interface stability in solid-state batteries, *Nature Reviews Materials* **5**, 105–126 (2019).
- [8] H. Yang and N. Wu, Ionic conductivity and ion transport mechanisms of solid-state lithium-ion battery electrolytes: A review, *Energy Science & Engineering* **10**, 1643 (2022).
- [9] W. D. Richards, L. J. Miara, Y. Wang, J. C. Kim, and G. Ceder, Interface stability in solid-state batteries, *Chemistry of Materials* **28**, 266 (2016).
- [10] R. Koerver, W. Zhang, L. d. Biasi, S. Schweidler, A. O. Kondrakov, S. Kolling, T. Brezesinski, P. Hartmann, W. G. Zeier, and J. Janek, Chemo-mechanical expansion of lithium electrode materials – on the route to mechanically optimized all-solid-state batteries, *Energy & Environmental Science* **11**, 2142 (2018).
- [11] A. Banerjee, X. Wang, C. Fang, E. A. Wu, and Y. S. Meng, Interfaces and interphases in all-solid-state batteries with inorganic solid electrolytes, *Chemical Reviews* **120**, 6878 (2020).
- [12] H. Xu, S. Yang, and B. Li, Pressure effects and countermeasures in solid-state batteries: A comprehensive review, *Advanced Energy Materials* **14**, 2303539 (2024).
- [13] X. Hu, Z. Zhang, X. Zhang, Y. Wang, X. Yang, X. Wang, M. Fayena-Greenstein, H. A. Yehezkel, S. Langford, D. Zhou, B. Li, G. Wang, and D. Aurbach, External-pressure–electrochemistry coupling in solid-state lithium metal batteries, *Nature Reviews Materials* **9**, 305 (2024).
- [14] Q. Li, H. Liu, Y. Ye, K. J. Li, F. Wu, L. Li, and R. Chen, The critical importance of stack pressure in batteries, *Nature Energy* **10**, 1064 (2025).
- [15] K. G. Naik, M. K. Jangid, B. S. Vishnugopi, N. P. Dasgupta, and P. P. Mukherjee, Interrogating the role of stack pressure in transport-reaction interaction in the solid-state battery cathode, *Advanced Energy Materials* **15**, 2403360 (2025).
- [16] M. Yang and Y. Mo, Interfacial defect of lithium metal in solid-state batteries, *Angewandte Chemie International Edition* **60**, 21494 (2021).
- [17] M. Zhao, J. Zhang, C. M. Costa, S. Lanceros-Méndez, Q. Zhang, and W. Wang, Unveiling challenges and opportunities in silicon-based all-solid-state batteries: Thin-film bonding with mismatch strain, *Advanced Materials* **36**, 2308590 (2024).
- [18] H.-C. Yu, D. Taha, T. Thompson, N. J. Taylor, A. Drews, J. Sakamoto, and K. Thornton, Deformation and stresses in solid-state composite battery cathodes, *Journal of Power Sources* **440**, 227116 (2019).
- [19] F. Al-Jaljouli, R. Mücke, C. Roitzheim, Y. J. Sohn, N. Yaqoob, M. Finsterbusch, P. Kaghazchi, and O. Guillon, Chemo-thermal stress in all-solid-state batteries: Impact of cathode active materials and microstructure, *Journal of Power Sources* **644**, 237136 (2025).
- [20] Y. He, C. Lu, S. Liu, W. Zheng, and J. Luo, Interfacial incompatibility and internal stresses in all-solid-state lithium ion batteries, *Advanced Energy Materials* **9**, 1901810 (2019).
- [21] P. Žgunc and B. Yildiz, Strain sensitivity of li-ion conductivity in  $\beta$ -li 3 ps 4 solid electrolyte, *PRX Energy* **1**, 023003 (2022).
- [22] Y. Gao, A. M. Nolan, P. Du, Y. Wu, C. Yang, Q. Chen, Y. Mo, and S.-H. Bo, Classical and emerging characterization techniques for investigation of ion transport mechanisms in crystalline fast ionic conductors, *Chemical Reviews* **120**, 5954 (2020).
- [23] T. Song, Y. Lin, D. Wang, Q. Chen, C. Ling, and S. Shi, Renewing fundamental understanding of ionic transport in inorganic crystalline solid-state electrolytes from the perspective of lattice dynamics, *Advanced Energy Materials* **14**, 2302440 (2024).
- [24] R. Li, S. Wen, K. Xu, C. Wang, Z. Lin, X. Tang, Z. Zhang, and Y.-S. Hu, Ultrahigh ionic conductivity in

- halide electrolytes enabled by anion framework flexibility engineering, *Journal of the American Chemical Society* 10.1021/jacs.5c15937 (2026).
- [25] T. Asano, A. Sakai, S. Ouchi, M. Sakaida, A. Miyazaki, and S. Hasegawa, Solid halide electrolytes with high lithium-ion conductivity for application in 4 v class bulk-type all-solid-state batteries, *Advanced Materials* 30, 1803075 (2018).
- [26] X. Li, J. Liang, X. Yang, K. R. Adair, C. Wang, F. Zhao, and X. Sun, Progress and perspectives on halide lithium conductors for all-solid-state lithium batteries, *Energy & Environmental Science* 13, 1429 (2020).
- [27] C. Wang, J. Liang, J. T. Kim, and X. Sun, Prospects of halide-based all-solid-state batteries: From material design to practical application, *Science Advances* 8, eadc9516 (2022).
- [28] R. Schlem, A. Banik, S. Ohno, E. Suard, and W. G. Zeier, Insights into the lithium sub-structure of superionic conductors  $\text{Li}_3\text{YCl}_6$  and  $\text{Li}_3\text{YBr}_6$ , *Chemistry of Materials* 33, 327 (2021).
- [29] J. Qi, S. Banerjee, Y. Zuo, C. Chen, Z. Zhu, M. H. Chandrappa, X. Li, and S. P. Ong, Bridging the gap between simulated and experimental ionic conductivities in lithium superionic conductors, *Materials Today Physics* 21, 100463 (2021).
- [30] R. Drautz, Atomic cluster expansion for accurate and transferable interatomic potentials, *Physical Review B* 99, 014104 (2019).
- [31] Y. Lysogorskiy, C. v. d. Oord, A. Bochkarev, S. Menon, M. Rinaldi, T. Hammerschmidt, M. Mrovec, A. Thompson, G. Csányi, C. Ortner, and R. Drautz, Performant implementation of the atomic cluster expansion (pace) and application to copper and silicon, *npj computational materials* 7, 97 (2021).
- [32] J. Klimeš, D. R. Bowler, and A. Michaelides, Van der waals density functionals applied to solids, *Physical Review B—Condensed Matter and Materials Physics* 83, 195131 (2011).
- [33] A. Bohnsack, F. Stenzel, A. Zajonc, G. Balzer, M. S. Wickleder, and G. Meyer, Ternäre halogenide vom typ  $\text{a}_3\text{mx}_6$ . vi [1]. ternäre chloride der selten-erd-elemente mit lithium,  $\text{Li}_3\text{mCl}_6$  ( $m = \text{tb-lu,y,sc}$ ): Synthese, kristallstrukturen und ionenbewegung, *Zeitschrift für anorganische und allgemeine Chemie* 623, 1067 (1997).
- [34] J. Liang, X. Li, K. R. Adair, and X. Sun, Metal halide superionic conductors for all-solid-state batteries, *Accounts of Chemical Research* 54, 1023 (2021).
- [35] J. Liang, E. van der Maas, J. Luo, X. Li, N. Chen, K. R. Adair, W. Li, J. Li, Y. Hu, J. Liu, L. Zhang, S. Zhao, S. Lu, J. Wang, H. Huang, W. Zhao, S. Parnell, R. I. Smith, S. Ganapathy, M. Wagemaker, and X. Sun, A series of ternary metal chloride superionic conductors for high-performance all-solid-state lithium batteries, *Advanced Energy Materials* 12, 2103921 (2022).
- [36] M. S. Daw and M. I. Baskes, Embedded-atom method: Derivation and application to impurities, surfaces, and other defects in metals, *Physical review B* 29, 6443 (1984).
- [37] M. S. Daw, S. M. Foiles, and M. I. Baskes, The embedded-atom method: a review of theory and applications, *Materials Science Reports* 9, 251 (1993).
- [38] G. Dusson, M. Bachmayr, G. Csányi, R. Drautz, S. Etter, C. van Der Oord, and C. Ortner, Atomic cluster expansion: Completeness, efficiency and stability, *Journal of Computational Physics* 454, 110946 (2022).
- [39] G. Kresse and J. Furthmüller, Efficient iterative schemes for ab initio total-energy calculations using a plane-wave basis set, *Physical review B* 54, 11169 (1996).
- [40] A. M. Ganose, H. Sahasrabudde, M. Asta, K. Beck, T. Biswas, A. Bonkowski, J. Bustamante, X. Chen, Y. Chiang, D. C. Chrzan, J. Clary, O. A. Cohen, C. Ertural, M. C. Gallant, J. George, S. Gerits, R. E. A. Goodall, R. D. Guha, G. Hautier, M. Horton, T. J. Inizan, A. D. Kaplan, R. S. Kingsbury, M. C. Kuner, B. Li, X. Linn, M. J. McDermott, R. S. Mohanakrishnan, A. N. Naik, J. B. Neaton, S. M. Parmar, K. A. Persson, G. Petretto, T. A. R. Purcell, F. Ricci, B. Rich, J. Riebesell, G.-M. Rignanese, A. S. Rosen, M. Scheffler, J. Schmidt, J.-X. Shen, A. Sobolev, R. Sundararaman, C. Tezak, V. Trinquet, J. B. Varley, D. Vigil-Fowler, D. Wang, D. Waroquiers, M. Wen, H. Yang, H. Zheng, J. Zheng, Z. Zhu, and A. Jain, Atomate2: modular workflows for materials science, *Digital Discovery* 4, 1944 (2025).
- [41] I. S. Novikov, K. Gubaev, E. V. Podryabinkin, and A. V. Shapeev, The mlip package: moment tensor potentials with mpi and active learning, *Machine Learning: Science and Technology* 2, 025002 (2020).
- [42] J. F. Nye, *Physical properties of crystals: their representation by tensors and matrices* (Oxford university press, 1985).
- [43] M. Wen, M. K. Horton, J. M. Munro, P. Huck, and K. A. Persson, An equivariant graph neural network for the elasticity tensors of all seven crystal systems, *Digital Discovery* 3, 869 (2024).
- [44] J. Qiu, M. Wu, W. Luo, B. Xu, G. Liu, and C. Ouyang, Insights into bulk properties and transport mechanisms in new ternary halide solid electrolytes: First-principles calculations, *The Journal of Physical Chemistry C* 125, 23510 (2021).
- [45] M. Jiang, S. Mukherjee, Z. W. Chen, L. X. Chen, M. L. Li, H. Y. Xiao, C. Gao, and C. V. Singh, Materials perspective on new lithium chlorides and bromides: insights into thermo-physical properties, *Physical Chemistry Chemical Physics* 22, 22758 (2020).
- [46] S. Wang, Q. Bai, A. M. Nolan, Y. Liu, S. Gong, Q. Sun, and Y. Mo, Lithium chlorides and bromides as promising solid-state chemistries for fast ion conductors with good electrochemical stability, *Angewandte Chemie International Edition* 58, 8039 (2019).
- [47] D. Park, H. Park, Y. Lee, S.-O. Kim, H.-G. Jung, K. Y. Chung, J. H. Shim, and S. Yu, Theoretical design of lithium chloride superionic conductors for all-solid-state high-voltage lithium-ion batteries, *ACS applied materials & interfaces* 12, 34806 (2020).
- [48] L. Hu, J. Zhu, C. Duan, J. Zhu, J. Wang, K. Wang, Z. Gu, Z. Xi, J. Hao, Y. Chen, J. Ma, J.-X. Liu, and C. Ma, Revealing the pnma crystal structure and ion-transport mechanism of the  $\text{Li}_3\text{YCl}_6$  solid electrolyte, *Cell Reports Physical Science* 10.1016/j.xcrp.2023.101428 (2023).
- [49] K. Kim, D. Park, H.-G. Jung, K. Y. Chung, J. H. Shim, B. C. Wood, and S. Yu, Material design strategy for halide solid electrolytes  $\text{Li}_3\text{Mx}_6$  ( $x = \text{cl, br, and i}$ ) for all-solid-state high-voltage li-ion batteries, *Chemistry of Materials* 33, 3669 (2021).
- [50] J. Geng, Z. Yan, and Y. Zhu, Elucidating anisotropic ionic diffusion mechanism in  $\text{Li}_3\text{YCl}_6$  with molecular dynamics simulations, *ACS Applied Energy Materials* 7, 7019 (2024).

- [51] S. Wang, Y. Liu, and Y. Mo, Frustration in super-ionic conductors unraveled by the density of atomistic states, *Angewandte Chemie* **135**, e202215544 (2023).
- [52] S. Plimpton, Fast parallel algorithms for short-range molecular dynamics, *Journal of computational physics* **117**, 1 (1995).
- [53] A. Einstein, Über die von der molekularkinetischen theorie der wärme geforderte bewegung von in ruhenden flüssigkeiten suspendierten teilchen, *Annalen der physik* **4**, 10.1002/andp.19053220806 (1905).
- [54] W. Nernst, Zur kinetik der in lösung befindlichen körper, *Zeitschrift für physikalische Chemie* **2**, 613 (1888).
- [55] R. Schlem, S. Muy, N. Prinz, A. Banik, Y. Shao-Horn, M. Zobel, and W. G. Zeier, Mechanochemical synthesis: a tool to tune cation site disorder and ionic transport properties of  $\text{Li}_3\text{MCl}_6$  ( $\text{M} = \text{Y}, \text{Er}$ ) superionic conductors, *Advanced Energy Materials* **10**, 1903719 (2020).
- [56] C. Chen, D. T. Nguyen, S. J. Lee, N. A. Baker, A. S. Karakoti, L. Lauw, C. Owen, K. T. Mueller, B. A. Bilodeau, V. Murugesan, and M. Troyer, Accelerating computational materials discovery with machine learning and cloud high-performance computing: from large-scale screening to experimental validation, *Journal of the American Chemical Society* **146**, 20009 (2024).
- [57] P. Qiu, Y. Chen, W. Wang, T. Liu, and J. Wu, A scalable and versatile synthetic strategy of halide electrolytes for high-performance all-solid-state lithium batteries, *ACS Applied Energy Materials* **8**, 6035 (2025).
- [58] J. Klimeš, D. R. Bowler, and A. Michaelides, Chemical accuracy for the van der waals density functional, *Journal of Physics: Condensed Matter* **22**, 022201 (2009).
- [59] S. Arrhenius, Über die reaktionsgeschwindigkeit bei der inversion von rohrzucker durch säuren, *Zeitschrift für physikalische Chemie* **4**, 226 (1889).
- [60] J. Lee, S. Ju, S. Hwang, J. You, J. Jung, Y. Kang, and S. Han, Disorder-dependent Li diffusion in  $\text{Li}_6\text{PS}_5\text{Cl}$  investigated by machine-learning potential, *ACS Applied Materials & Interfaces* **16**, 46442 (2024).
- [61] E. Van Der Maas, W. Zhao, Z. Cheng, T. Famprakis, M. Thijs, S. R. Parnell, S. Ganapathy, and M. Wage-maker, Investigation of structure, ionic conductivity, and electrochemical stability of halogen substitution in solid-state ion conductor  $\text{Li}_3\text{YBr}_x\text{Cl}_{6-x}$ , *The Journal of Physical Chemistry C* **127**, 125 (2022).
- [62] J. P. Perdew, A. Ruzsinszky, G. I. Csonka, O. A. Vydrov, G. E. Scuseria, L. A. Constantin, X. Zhou, and K. Burke, Restoring the density-gradient expansion for exchange in solids and surfaces, *Physical review letters* **100**, 136406 (2008).
- [63] T. Ayadi, M. Nastar, and F. Bruneval, Structural and thermodynamic properties of the  $\text{Li}_6\text{PS}_5\text{Cl}$  solid electrolyte using first-principles calculations, *Journal of Materials Chemistry A* **12**, 33723 (2024).
- [64] T. Gould, S. Lebegue, J. G. Angyan, and T. Bučko, A fractionally ionic approach to polarizability and van der waals many-body dispersion calculations, *Journal of chemical theory and computation* **12**, 5920 (2016).
- [65] T. Krauskopf, H. Hartmann, W. G. Zeier, and J. Janek, Toward a fundamental understanding of the lithium metal anode in solid-state batteries—an electrochemomechanical study on the garnet-type solid electrolyte  $\text{Li}_6\text{Zn}_2\text{Al}_2\text{O}_{12}$ , *ACS applied materials & interfaces* **11**, 14463 (2019).
- [66] M. Yang, Y. Liu, A. M. Nolan, and Y. Mo, Interfacial atomistic mechanisms of lithium metal stripping and plating in solid-state batteries, *Advanced Materials* **33**, 2008081 (2021).
- [67] L. Zhao, W. Li, C. Wu, Q. Ai, L. Guo, S. Chen, J. Zheng, M. Anderson, H. Guo, J. Lou, Y. Liang, Z. Fan, J. Zhu, and Y. Yao, Taming metal–solid electrolyte interface instability via metal strain hardening, *Advanced Energy Materials* **13**, 2300679 (2023).
- [68] J.-M. Doux, Y. Yang, D. H. Tan, H. Nguyen, E. A. Wu, X. Wang, A. Banerjee, and Y. S. Meng, Pressure effects on sulfide electrolytes for all solid-state batteries, *Journal of Materials Chemistry A* **8**, 5049 (2020).
- [69] J. Janek and W. G. Zeier, Challenges in speeding up solid-state battery development, *Nature Energy* **8**, 230 (2023).
- [70] P. G. Shewmon, *Diffusion in Solids*, The Minerals, Metals & Materials Series (Springer International Publishing, 2016).

**Supplemental Material:**  
**Strain-Dependent Ionic Transport in  $\text{Li}_3\text{YCl}_6$  Solid  
Electrolytes**

Wei-Fan Huang,<sup>1</sup> Jin Dai,<sup>1</sup> Jiahui Pan,<sup>2</sup> and Mingjian Wen<sup>2,\*</sup>

<sup>1</sup>*William A. Brookshire Department of Chemical and Biomolecular Engineering,  
University of Houston, Houston, TX, 77204, USA*

<sup>2</sup>*Institute of Fundamental and Frontier Sciences,  
University of Electronic Science and Technology of China, Chengdu, 611731, China*

# 1. ACE MODEL DEVELOPMENT

## 1.1. AIMD Training Data Selection

Since successive snapshots in AIMD trajectories are highly correlated, we subsampled the trajectory to retain only representative configurations. To this end, we used DDescribe [1] to convert each snapshot into a Smooth Overlap of Atomic Positions (SOAP) [2] vector, which encodes the local atomic environment in a continuous and invariant representation. KMeans clustering was then applied in SOAP space to identify and extract 200 representative configurations, as shown in Fig. S1, with PCA used to reduce the dimensionality for visualization [3].

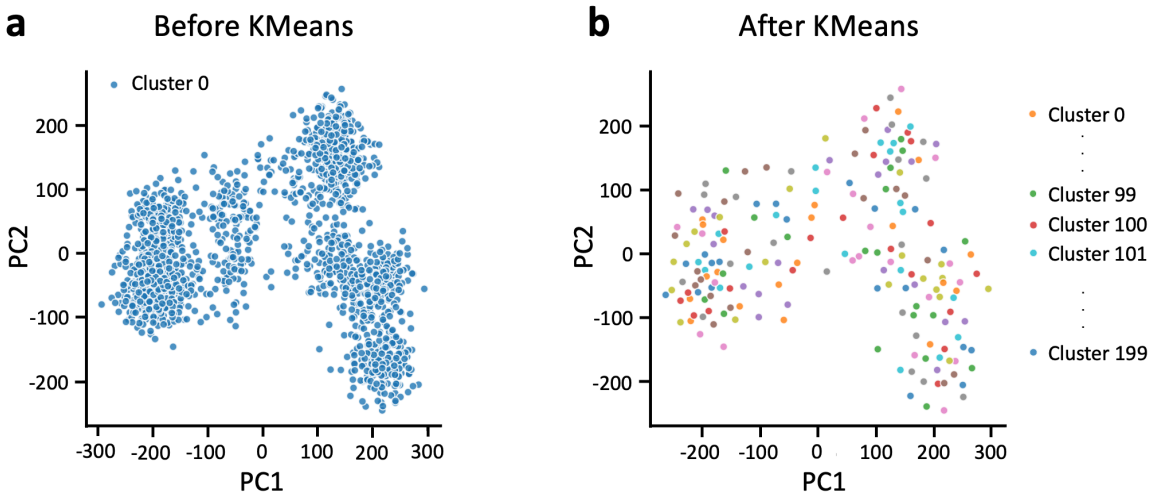


FIG. S1: **Data selection using KMeans clustering.** Data points from MD at 550 K for  $\text{Li}_3\text{YCl}_6$  ( $\text{P}\bar{3}\text{m1}$ ), shown (a) before and (b) after KMeans clustering.

## 1.2. Model Training and Hyperparameter Tuning

The ACE model was trained by minimizing a loss function that balances energy and force predictions with regularizations that enforce the smoothness of the potential energy

\* mjwen@uestc.edu.cn

surface [4]:

$$\begin{aligned}
\mathcal{L} &= (1 - \kappa)\Delta_E^2 + \kappa\Delta_F^2 + \Delta_{coeff} + \Delta_{rad} \\
\Delta_{coeff} &= L_1 \sum_{p\mu n\mathbf{L}} \left| c_{\mu n\mathbf{L}}^{(p)} \right| + L_2 \sum_{p\mu n\mathbf{L}} \left| c_{\mu n\mathbf{L}}^{(p)} \right|^2 \\
\Delta_{rad} &= \frac{w_0}{r_{cut}^2} \int r^2 \sum_{nl} |R_{nl}(r)| dr + \frac{w_1}{r_{cut}^2} \int r^2 \sum_{nl} \left| \frac{dR_{nl}(r)}{dr} \right| dr + \frac{w_2}{r_{cut}^2} \int r^2 \sum_{nl} \left| \frac{d^2 R_{nl}(r)}{dr^2} \right| dr
\end{aligned} \tag{1}$$

where  $\kappa$  controls the relative weight of energy ( $\Delta_E^2$ ) and force ( $\Delta_F^2$ ) errors;  $\Delta_{coeff}$  applies  $L_1/L_2$  regularization on the expansion coefficients  $c_{\mu n\mathbf{L}}^{(p)}$ ; and  $\Delta_{rad}$  penalizes the zeroth, first, and second derivatives of the radial basis functions  $R_{nl}(r)$  with weights  $w_0, w_1, w_2$ , promoting smoothness up to second order. Omitting regularization leads to a poor description of high-energy configurations. The used values are listed in Table S1.

TABLE S1: Hyperparameters for the ACE model training.

$\kappa$	$L_1$	$L_2$	$w_0$	$w_1$	$w_2$	$r_{cut}$	<code>maxiter</code>	<code>ladder_step</code>
0.35	$1 \times 10^{-8}$	$1 \times 10^{-8}$	$1 \times 10^{-8}$	$1 \times 10^{-8}$	$1 \times 10^{-8}$	7.000 Å	200	12

The hyperparameters `maxiter` and `ladder_step` were tuned with results shown in Fig. S2. `ladder_step` controls how many basis functions are added per iteration: smaller values introduce fewer functions at each step, enabling more careful optimization at the cost of longer training times, but with negligible effect on energy errors. Conversely, increasing `maxiter` reduces force errors with little impact on energy accuracy, at the expense of greater computational cost. A balance between accuracy and efficiency was achieved with `maxiter` = 200 and `ladder_step` = 12.

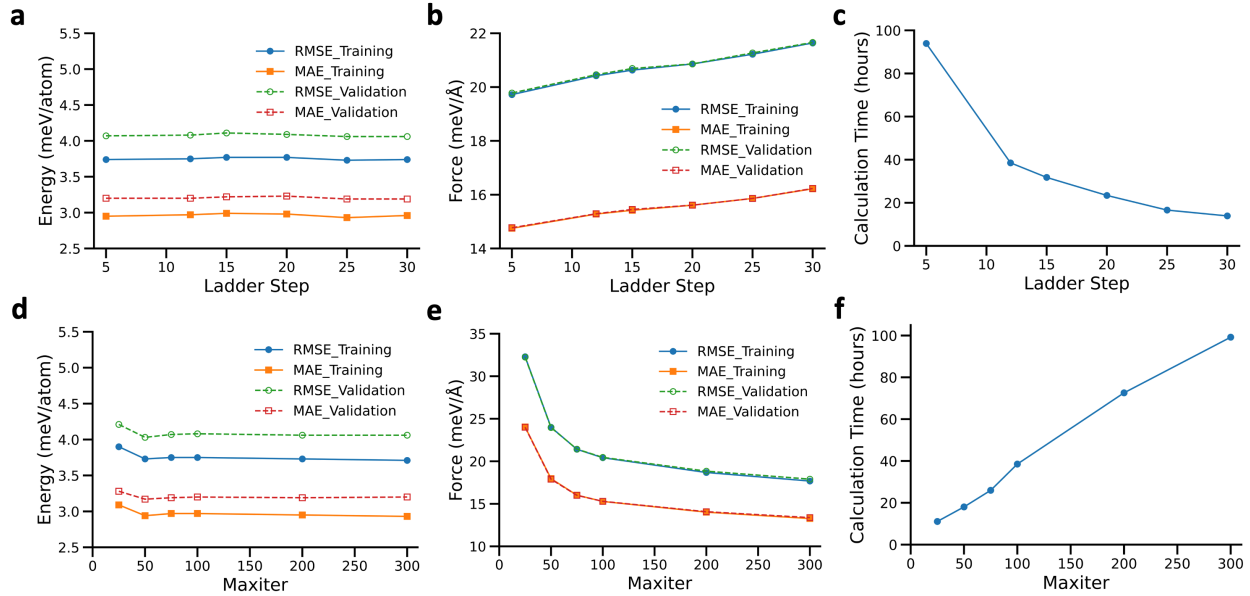


FIG. S2: **Hyperparameter tuning error metrics.** (a)–(c) Energy/force RMSE and MAE, and computation time vs. ladder\_step (maxiter = 100). (d)–(f) Same metrics vs. maxiter (ladder\_step = 12).

## 2. MODEL PERFORMANCE

TABLE S2: **Error metrics of 1st to 4th ACE model.** Root-mean-square error (RMSE) and mean absolute error (MAE) for energy (meV/atom) and forces (meV/Å) across training, validation, and test sets. Each model corresponds to a different round of active learning (AL).

		1st (Before AL)		2nd (After 1st AL)		3rd (After 2nd AL)		4th (After 3rd AL)				
Dataset	Metric	Energy	Force	Metric	Energy	Force	Metric	Energy	Force	Metric	Energy	Force
Training	RMSE	0.55	16.02	RMSE	0.58	16.70	RMSE	0.63	17.09	RMSE	0.64	17.96
	MAE	0.45	11.98	MAE	0.47	12.40	MAE	0.51	12.57	MAE	0.51	13.10
Validation	RMSE	0.59	16.37	RMSE	0.61	16.75	RMSE	0.64	16.98	RMSE	0.65	18.01
	MAE	0.50	12.20	MAE	0.50	12.40	MAE	0.52	12.44	MAE	0.50	13.08
Test	RMSE	0.55	16.51	RMSE	0.56	17.06	RMSE	0.63	17.39	RMSE	0.67	18.44
	MAE	0.46	12.34	MAE	0.47	12.61	MAE	0.48	14.12	MAE	0.53	13.48

TABLE S3: **Error metrics of 5th to 8th ACE model.** RMSE and MAE for energy (meV/atom) and forces (meV/Å) across training, validation, and test sets. Each model corresponds to a different round of active learning (AL). The numbers in parentheses indicate changes relative to the 1st model.

		5th (After 4th AL)		6th (After 5th AL)		7th (After 6th AL)		8th (After 7th AL)				
Dataset	Metric	Energy	Force	Metric	Energy	Force	Metric	Energy	Force	Metric	Energy	Force
Training	RMSE	0.62	18.71	RMSE	0.63	18.73	RMSE	0.70	19.24	RMSE	0.67 (+0.08)	19.18 (+3.16)
	MAE	0.48	13.69	MAE	0.48	13.70	MAE	0.54	14.05	MAE	0.52 (+0.07)	13.99 (+2.01)
Validation	RMSE	0.63	18.71	RMSE	0.64	18.74	RMSE	0.68	19.26	RMSE	0.67 (+0.08)	19.24 (+2.87)
	MAE	0.46	13.68	MAE	0.47	13.69	MAE	0.53	14.03	MAE	0.51 (+0.01)	14.02 (+1.82)
Test	RMSE	0.63	19.03	RMSE	0.64	19.35	RMSE	0.68	19.33	RMSE	0.67 (+0.12)	19.23 (+2.72)
	MAE	0.48	13.97	MAE	0.49	14.16	MAE	0.53	14.13	MAE	0.52 (+0.06)	14.09 (+1.75)

TABLE S4: **Error metrics of ACE model trained on DFT data generated with the PBEsol functional.** Root-mean-square error (RMSE) and mean absolute error (MAE) for energy (meV/atom) and forces (meV/Å) across training, validation, and test sets.

Dataset	Metric	Energy	Force
Training	RMSE	0.73	20.27
	MAE	0.59	14.78
Validation	RMSE	0.71	20.18
	MAE	0.58	14.77
Test	RMSE	0.71	20.18
	MAE	0.58	14.77

### 3. LI<sup>+</sup> PROBABILITY DENSITY

The Li<sup>+</sup> probability density maps were computed from 500 ps MD simulations employing the `pymatgen-analysis-diffusion` package [5, 6] to map the trajectory-derived ionic density onto a real-space grid. The probability density  $\rho(\mathbf{r})$  reflects the time-averaged likelihood of finding a Li<sup>+</sup> ion at a given position  $\mathbf{r}$  in the simulation cell, constructed by accumulating ionic positions across all MD snapshots onto a uniform grid with a spatial interval of 0.5 Å.

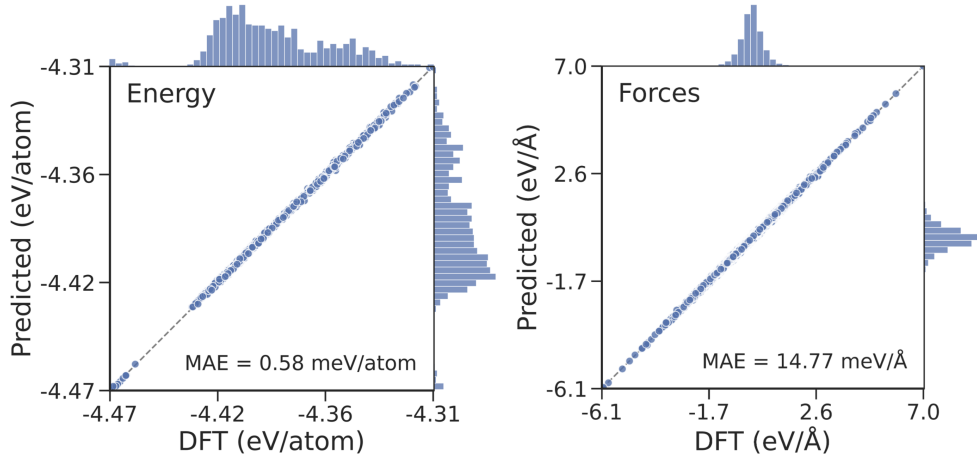


FIG. S3: Comparison between DFT (PBEsol) and ACE model predictions for energy and forces on the test set. The ACE model was trained on data generated with the PBEsol functional.

Regions of high  $\rho(\mathbf{r})$  correspond to preferred  $\text{Li}^+$  residence sites and low-barrier migration pathways, providing an intuitive visualization of the diffusion landscape. The isosurfaces shown in the main text correspond to a level of  $5 \times 10^{-5} \text{ e/Bohr}^3$ , chosen to highlight the interconnected network of  $\text{Li}^+$  conduction channels while suppressing low-occupancy regions. The probability density maps are provided in Fig. S4 and Fig. S5 for the  $\text{P}\bar{3}\text{m1}$  and  $\text{Pnma}$  phases, respectively.

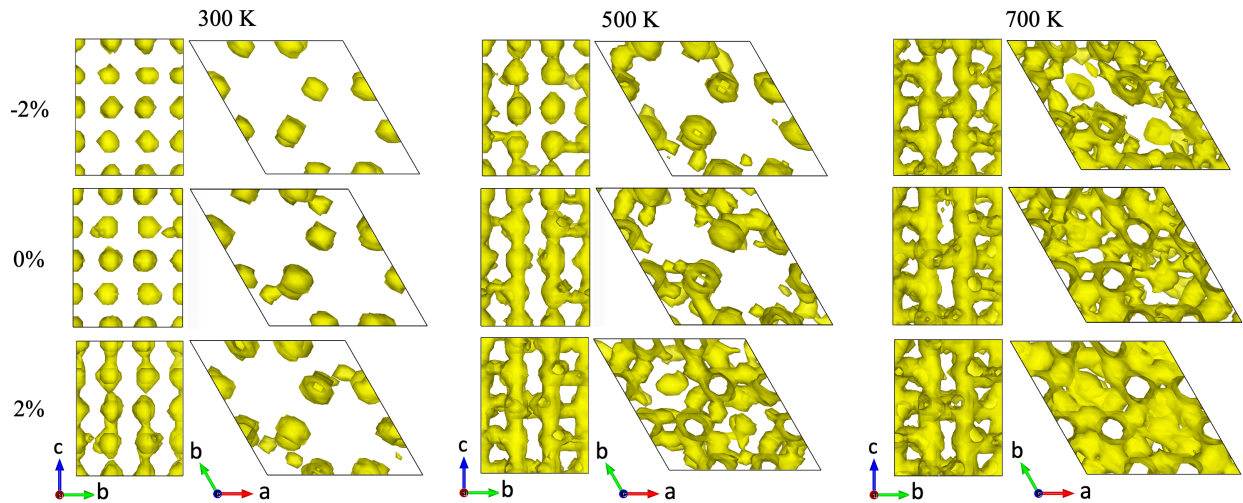


FIG. S4:  $\text{Li}^+$  probability density in  $\text{Li}_3\text{YCl}_6$  ( $\text{P}\bar{3}\text{m1}$ ) under various strain conditions.

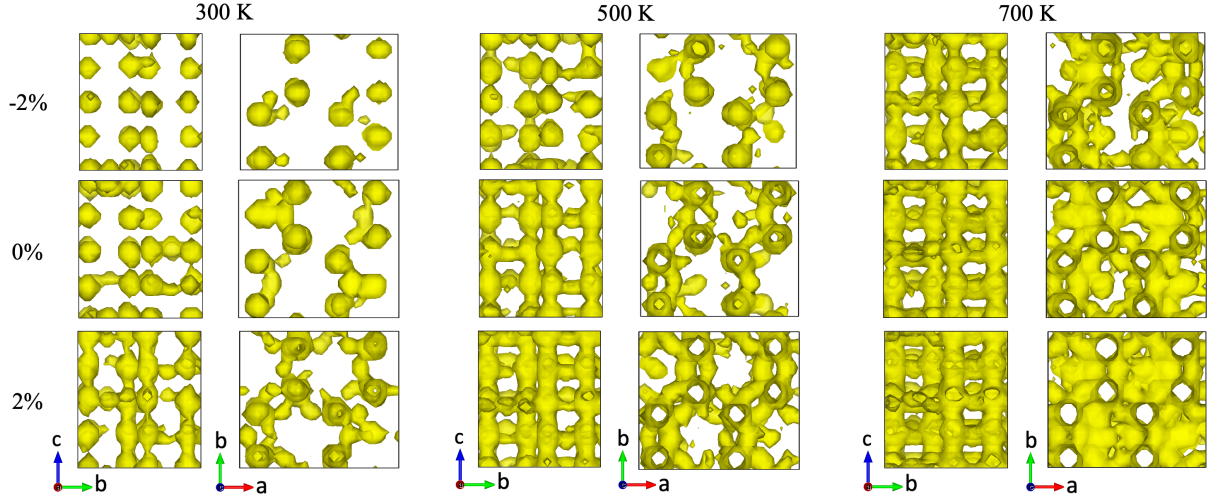


FIG. S5:  $\text{Li}^+$  probability density in  $\text{Li}_3\text{YCl}_6$  (Pnma) under various strain conditions.

To characterize the anisotropy of  $\text{Li}^+$  diffusion, we plot the ratio  $D_{xy}/D_z$  for different DFT functionals in Fig. S6. At low temperatures,  $\text{Li}^+$  migration is primarily restricted to the  $z$ -axis via the Oct–Oct pathway, yielding  $D_{xy}/D_z \ll 1$ . Above the critical temperature  $T_c$ , activation of the Oct–Tet–Oct pathway drives  $D_{xy}/D_z$  toward unity, signaling the onset of three-dimensional cooperative diffusion.

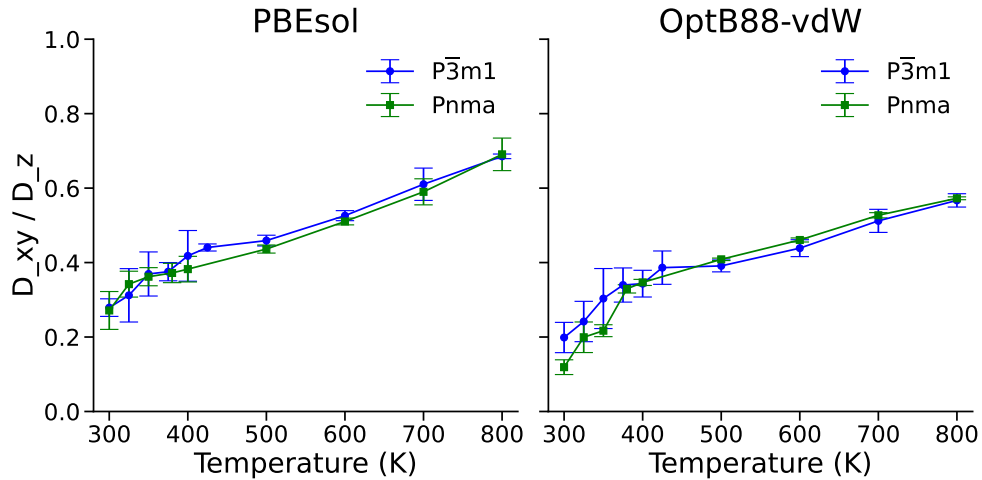


FIG. S6: Diffusivity ratio of  $\text{Li}^+$  along different directions.

#### 4. $\text{Li}^+$ SITE OCCUPANCY

To quantify the dynamic distribution of  $\text{Li}^+$  ions, we analyzed the local coordination environment based on the distance between each  $\text{Li}^+$  and its neighbors throughout the MD trajectories. The coordination number ( $CN$ ) of a  $\text{Li}^+$  ion is defined as the total count of  $\text{Cl}^-$  and  $\text{Y}^{3+}$  neighbors within a specific cutoff radius of  $3.5 \text{ \AA}$ .

The sites are categorized into four groups based on  $CN$ : octahedral ( $CN = 6$ ), tetrahedral ( $CN = 4$ ), intermediate ( $CN = 5$ ), and others ( $CN = 3, 7-9$ ). The occupancy for each site type  $k$  is defined as the fraction of  $\text{Li}^+$  ions found in that environment across all sampled frames:

$$\text{Site Fraction}_k = \frac{\sum_{t=1}^{N_{\text{frames}}} N_{k,t}}{N_{\text{total}} \times N_{\text{frames}}} \times 100\% \quad (2)$$

where  $N_{k,t}$  is the number of  $\text{Li}^+$  ions in type  $k$  at frame  $t$ ,  $N_{\text{total}}$  is the number of  $\text{Li}^+$  ions in the simulation cell, and  $N_{\text{frames}}$  is the total number of MD frames analyzed.

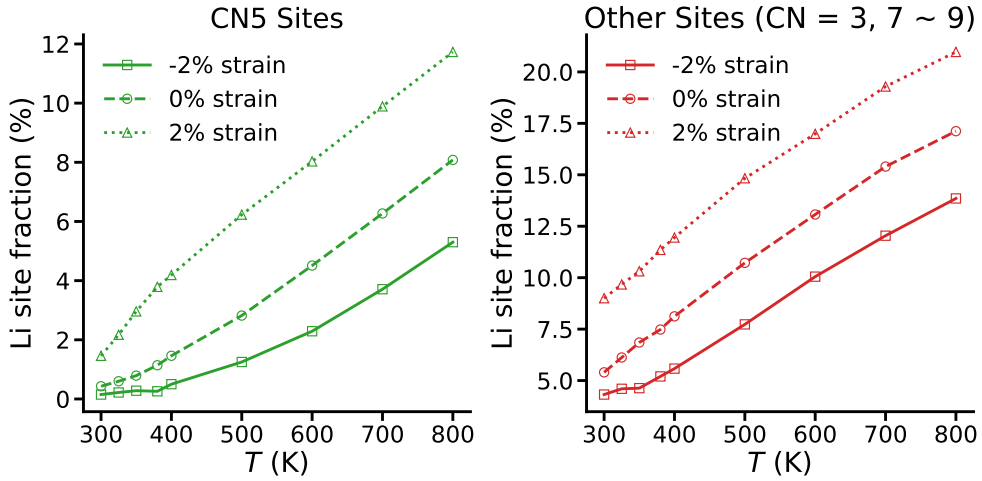


FIG. S7:  $\text{Li}^+$  site occupancy for the  $CN = 5$  and other coordination numbers.

#### 5. ELASTIC MODULI

Given the elastic tensor components  $C_{ij}$  obtained from DFT calculations or interatomic potentials, the bulk modulus ( $K$ ), shear modulus ( $G$ ), and Young's modulus ( $E$ ) can be computed as averaged measures for polycrystalline materials, reflecting the overall elastic response. There are three common averaging schemes. In the Voigt approach, uniform strain

is assumed across all grains, yielding upper-bound estimates of the moduli. In the Reuss approach, uniform stress is assumed, yielding lower-bound estimates. The Hill approach takes the arithmetic mean of the Voigt and Reuss values and provides a more accurate representation [7, 8].

$$\begin{aligned}
K_V &= \frac{C_{11} + C_{22} + C_{33} + 2(C_{12} + C_{23} + C_{13})}{9}, \\
G_V &= \frac{C_{11} + C_{22} + C_{33} - C_{12} - C_{23} - C_{13} + 3(C_{44} + C_{55} + C_{66})}{15} \\
K_R &= \frac{1}{S_{11} + S_{22} + S_{33} + 2(S_{12} + S_{23} + S_{13})}, \\
G_R &= \frac{15}{4(S_{11} + S_{22} + S_{33}) - 4(S_{12} + S_{23} + S_{13}) + 3(S_{44} + S_{55} + S_{66})}, \\
K_H &= \frac{K_V + K_R}{2}, \quad G_H = \frac{G_V + G_R}{2}.
\end{aligned} \tag{3}$$

In all three schemes, the elastic moduli can be obtained as  $E = 9KG/(3K + G)$  by using the corresponding  $K$  and  $G$  values. Here,  $S_{ij}$  denotes the components of the compliance tensor, obtained as the inverse of the elastic tensor:  $\mathbf{S} = \mathbf{C}^{-1}$ . The reported bulk, shear, and Young's moduli in this work were calculated using the Hill averaging scheme.

## 6. STRESS UNDER ISOTROPIC STRAIN

For an isotropic strain of 2%, the strain vector in Voigt notation is  $\boldsymbol{\varepsilon} = (0.02, 0.02, 0.02, 0, 0, 0)^\top$ , and the stress follows from  $\boldsymbol{\sigma} = \mathbf{C}\boldsymbol{\varepsilon}$ . Using the elastic tensor values from Table II in the main text, we compute the stress. For the  $P\bar{3}m1$  phase,

$$\begin{pmatrix} \sigma_1 \\ \sigma_2 \\ \sigma_3 \\ \sigma_4 \\ \sigma_5 \\ \sigma_6 \end{pmatrix} = \begin{pmatrix} 54.7 & 20.4 & 13.1 & -1.7 & 0 & 0 \\ 20.4 & 54.7 & 13.1 & 1.7 & 0 & 0 \\ 13.1 & 13.1 & 41.4 & 0 & 0 & 0 \\ -1.7 & 1.7 & 0 & 13.7 & 0 & 0 \\ 0 & 0 & 0 & 0 & 13.7 & -1.7 \\ 0 & 0 & 0 & 0 & -1.7 & 17.2 \end{pmatrix} \begin{pmatrix} 0.02 \\ 0.02 \\ 0.02 \\ 0 \\ 0 \\ 0 \end{pmatrix} = \begin{pmatrix} 1.764 \\ 1.764 \\ 1.352 \\ 0 \\ 0 \\ 0 \end{pmatrix} \text{ GPa.} \tag{4}$$

The maximum stress is  $\sigma_1 = \sigma_2 = 1.764$  GPa, attained in the basal plane, while the  $c$ -axis component  $\sigma_3 = 1.352$  GPa is about 23% smaller, reflecting the softer  $C_{33}$ .

For the Pnma phase,

$$\begin{pmatrix} \sigma_1 \\ \sigma_2 \\ \sigma_3 \\ \sigma_4 \\ \sigma_5 \\ \sigma_6 \end{pmatrix} = \begin{pmatrix} 53.5 & 19.0 & 12.3 & 0 & 0 & 0 \\ 19.0 & 52.9 & 12.5 & 0 & 0 & 0 \\ 12.3 & 12.5 & 38.6 & 0 & 0 & 0 \\ 0 & 0 & 0 & 12.9 & 0 & 0 \\ 0 & 0 & 0 & 0 & 11.6 & 0 \\ 0 & 0 & 0 & 0 & 0 & 16.9 \end{pmatrix} \begin{pmatrix} 0.02 \\ 0.02 \\ 0.02 \\ 0 \\ 0 \\ 0 \end{pmatrix} = \begin{pmatrix} 1.696 \\ 1.688 \\ 1.268 \\ 0 \\ 0 \\ 0 \end{pmatrix} \text{ GPa.} \quad (5)$$

The maximum stress is  $\sigma_1 = 1.696$  GPa along the  $a$  axis, narrowly exceeding  $\sigma_2 = 1.688$  GPa along  $b$ , while  $\sigma_3 = 1.268$  GPa along  $c$  is again the smallest by roughly 25%.

## 7. IONIC CONDUCTIVITY

The  $\text{Li}^+$  diffusivity  $D$  is extracted from MD trajectories using the Einstein relation [9], which connects the mean squared displacement (MSD) of the mobile ions to  $D$ :

$$D = \frac{1}{2dNt} \sum_{i=1}^N \langle |\mathbf{r}_i(t) - \mathbf{r}_i(0)|^2 \rangle \quad (6)$$

where  $N$  is the number of mobile ions,  $d$  is the system dimensionality (typically  $d = 3$ ), and  $\mathbf{r}_i(t)$  is the position vector of ion  $i$  at time  $t$ .  $D$  is obtained by linear regression of the MSD versus time within the diffusive regime, where the slope is proportional to  $2dD$ .

The ionic conductivity  $\sigma$  is then derived from  $D$  via the Nernst–Einstein equation [10]:

$$\sigma = \frac{N}{V} \frac{q^2}{k_B T} D \quad (7)$$

where  $q$  is the charge of the carrier,  $V$  is the volume of the simulation cell,  $k_B$  is the Boltzmann constant, and  $T$  is the temperature.

## REFERENCES

- [1] L. Himanen, M. O. Jäger, E. V. Morooka, F. F. Canova, Y. S. Ranawat, D. Z. Gao, P. Rinke, and A. S. Foster, Dscribe: Library of descriptors for machine learning in materials science, *Computer Physics Communications* **247**, 106949 (2020).
- [2] A. P. Bartók, R. Kondor, and G. Csányi, On representing chemical environments, *Phys. Rev. B* **87**, 184115 (2013).

- [3] S. Roweis, Em algorithms for pca and spca, *Advances in neural information processing systems* **10** (1997).
- [4] A. Bochkarev, Y. Lysogorskiy, S. Menon, M. Qamar, M. Mrovec, and R. Drautz, Efficient parametrization of the atomic cluster expansion, *Physical Review Materials* **6**, 013804 (2022).
- [5] Z. Deng, Z. Zhu, I.-H. Chu, and S. P. Ong, Data-driven first-principles methods for the study and design of alkali superionic conductors, *Chemistry of Materials* **29**, 281–288 (2016).
- [6] S. P. Ong, W. D. Richards, A. Jain, G. Hautier, M. Kocher, S. Cholia, D. Gunter, V. L. Chevrier, K. A. Persson, and G. Ceder, Python materials genomics (pymatgen): A robust, open-source python library for materials analysis, *Computational Materials Science* **68**, 314–319 (2013).
- [7] J. F. Nye, *Physical properties of crystals: their representation by tensors and matrices* (Oxford university press, 1985).
- [8] M. Wen, M. K. Horton, J. M. Munro, P. Huck, and K. A. Persson, An equivariant graph neural network for the elasticity tensors of all seven crystal systems, *Digital Discovery* **3**, 869 (2024).
- [9] A. Einstein, Über die von der molekularkinetischen theorie der wärme geforderte bewegung von in ruhenden flüssigkeiten suspendierten teilchen, *Annalen der physik* **4**, 10.1002/andp.19053220806 (1905).
- [10] W. Nernst, Zur kinetik der in lösung befindlichen körper, *Zeitschrift für physikalische Chemie* **2**, 613 (1888).